ADAPTIVE DISCONTINUOUS GALERKIN FINITE ELEMENT METHODS FOR NONLINEAR HYPERBOLIC CONSERVATION LAWS

RALF HARTMANN* AND PAUL HOUSTON†

Abstract. We consider the *a posteriori* error analysis and adaptive mesh design for discontinuous Galerkin finite element approximations to systems of nonlinear hyperbolic conservation laws. In particular, we discuss the question of error estimation for general linear and nonlinear functionals of the solution; typical examples include the outflow flux, local average and pointwise value, as well as the lift and drag coefficients of a body immersed in an inviscid fluid. By employing a duality argument, we derive so-called weighted or Type I *a posteriori* error bounds; in these error estimates the element–residuals are multiplied by local weights involving the solution of a certain dual problem. Based on these *a posteriori* bounds, we design and implement the corresponding adaptive algorithm to ensure efficient and reliable control of the error in the computed functional. The theoretical results are illustrated by a series of numerical experiments. In particular, we demonstrate the superiority of the proposed approach over standard mesh refinement algorithms which employ *ad hoc* error indicators.

Key words. Discontinuous Galerkin, *a posteriori* error analysis, adaptivity, nonlinear hyperbolic conservation laws

AMS subject classifications. AMS(MOS) 65N12, 65N15, 65N30

1. Introduction.

The ever–increasing range of applications of compressible fluid dynamics is a fertile source of difficult and challenging problems with important implications in engineering design. Multi-dimensional compressible flows are modelled by nonlinear conservation laws whose solutions exhibit a wide range of localised structures, such as shock waves, contact discontinuities and rarefaction waves. The accurate numerical resolution of these features necessitates the use of locally refined, adaptive computational meshes. The majority of adaptive algorithms used in computational fluid dynamics applications will simply refine or adjust the mesh according to an *ad hoc* criterion, such as a large gradient in a physical quantity or the size of the local residual, for example. Although this intuitive approach has had some success, it does not provide guaranteed error control. Moreover, *ad hoc* refinement strategies may not provide the most economical mesh design for the control of a given error quantity of interest, cf. [17, 20, 21, 28, 29], for example.

In this paper we consider the *a posteriori* error analysis and adaptive mesh design for discontinuous Galerkin finite element approximations to systems of nonlinear hyperbolic conservation laws. In particular, we shall be concerned with the derivation of computable error bounds for arbitrary linear and nonlinear functionals of the solution of practical interest; relevant examples include the lift and drag coefficients of a body immersed into an inviscid fluid, the local mean value of the field or its flux through the outflow boundary of the computational domain, and the pointwise evaluation of a component of the solution vector at a given point in the computational domain.

By employing a duality argument we derive so–called weighted, or Type I (cf. [23], for example), *a posteriori* estimates which bound the error between the true value of the prescribed functional, and the actual computed value. In these error

*Institute of Applied Mathematics, University of Heidelberg, Im Neuenheimer Feld 293, D-69120 Heidelberg, Germany (e-mail: Ralf.Hartmann@iwr.uni-heidelberg.de).

†Department of Mathematics & Computer Science, University of Leicester, Leicester LE1 7RH, UK (e-mail: Paul.Houston@mcs.le.ac.uk).

estimates, the element residuals of the computed numerical solution are multiplied by local weights involving the solution of a certain *dual* or *adjoint* problem. These weights represent the sensitivity of the relevant error quantity with respect to variations of the local element residuals. Since the solution to the dual problem is usually unknown analytically, it has to be approximated numerically as part of the error estimation process. However, the cost of this additional calculation is in general relatively cheap in comparison to the cost of determining the numerical approximation to the original (primal) system of nonlinear conservation laws, since the dual problem comprises of a system of *linear* partial differential equations. On the basis of the resulting *a posteriori* error estimate, the mesh is locally adapted and a new approximation to the primal and dual solution is computed. This feed-back algorithm is repeated until the error in the prescribed functional is below some user–defined tolerance, for example. This procedure leads to optimal finite element meshes which are specifically tailored to the accurate computation of the selected target functional. For related work in this area, we refer to the review article by Rannacher [28].

The paper is structured as follows. After introducing, in Section 2, our model system of nonlinear hyperbolic conservation laws, in Section 3, we formulate its discontinuous Galerkin finite element approximation. Then, in Section 4 we derive *a posteriori* error bounds for general linear and nonlinear functionals of the solution. Our *a posteriori* error bounds stem from a hyperbolic duality argument and include computable residual terms multiplied by local weights involving the (unknown) dual solution. Thereby, in Section 5, we discuss how the dual problem may be numerically approximated without compromising the reliability of the underlying error bound. On the basis of the resulting *a posteriori* error bound, in Section 6, we design and implement the corresponding adaptive algorithm to ensure both the reliable and efficient control of the error in the prescribed functional. The performance of this refinement strategy is then studied in Section 7 through a series of numerical experiments. In particular, we demonstrate the superiority of using our weighted *a posteriori* error indicators over traditional *ad hoc* error indicators which do not require the solution of an auxiliary or dual problem. Finally, in Section 8 we summarise the work presented in this paper and draw some conclusions.

The work presented in this paper is a complete and improved account of our recent work announced in the conference papers [17, 20].

2. Model problem. Given a final time $T > 0$, we consider the following system of conservation laws

$$\begin{aligned} \partial_t \mathbf{u} + \sum_{i=1}^{d} \frac{\partial}{\partial x_i} \mathbf{f}_i(\mathbf{u}) &= 0 \qquad \text{in } (0,T] \times \mathbb{R}^d, \\ \mathbf{u}(0,\cdot) &= \mathbf{u}_0(\cdot) \quad \text{in } \mathbb{R}^d, \end{aligned} \tag{2.1}$$

where $d \geq 1$, $\mathbf{u} = (u_1, \ldots, u_m)^T$ and $\mathbf{f}_i : \mathbb{R}^m \to \mathbb{R}^m$, $i = 1, \ldots, d$, are continuously differentiable. We note that (2.1) is hyperbolic, when

$$A(\mathbf{u}, \nu) := \sum_{i=1}^{d} \nu_i A_i(\mathbf{u})$$

has m real eigenvalues and a complete set of linearly independent eigenvectors for all vectors $\nu = (\nu_1, \ldots, \nu_d) \in \mathbb{R}^d$. Here, the $A_i(\mathbf{u})$ denote the Jacobi matrices of the fluxes $\mathbf{f}_i(\mathbf{u})$, respectively, $i = 1, \ldots, d$; i.e.

$$A_i(\mathbf{u}) := \nabla_{\mathbf{u}} \mathbf{f}_i(\mathbf{u}). \tag{2.2}$$

An important example of such a model problem is represented by the Euler equations of compressible gas dynamics. In two space–dimensions, the state vector $\mathbf{u} = (\rho, \rho u, \rho v, \rho E)$, where ρ, (u, v) and E represent the density, Cartesian velocity and total energy per unit mass, respectively. Furthermore, the fluxes are defined by

$$\mathbf{f}_1 = \begin{bmatrix} \rho u \\ \rho u^2 + p \\ \rho uv \\ \rho H u \end{bmatrix} \quad \text{and} \quad \mathbf{f}_2 = \begin{bmatrix} \rho v \\ \rho uv \\ \rho v^2 + p \\ \rho H v \end{bmatrix},$$

respectively. Here, p denotes the pressure, while H is the total enthalpy defined by

$$H = E + \frac{p}{\rho}.$$

The equation of state of an ideal gas is given by

$$p = (\gamma - 1)\rho \left(E - \frac{1}{2}(u^2 + v^2) \right), \tag{2.3}$$

where γ is the ratio of specific heats which, for dry air, is $\gamma = 1.4$.

For simplicity, we shall assume that the solution $\mathbf{u}$ of (2.1) remains constant outside some bounded region $\Omega \subset \mathbb{R}^d$, with boundary Γ, and confine ourselves to this finite domain. In this case the system of conservation laws (2.1) must be supplemented by appropriate boundary conditions; for example at inflow/outflow boundaries, we require that

$$A^-(\mathbf{u}, \mathbf{n})\,(\mathbf{u} - \mathbf{g}) = \mathbf{0}, \tag{2.4}$$

where $\mathbf{n}$ denotes the unit outward normal vector to the boundary Γ and $\mathbf{g}$ is a (given) real–valued vector function. Here, $A^-(\mathbf{u}, \mathbf{n})$ denotes the negative part of $A(\mathbf{u}, \mathbf{n})$; i.e.

$$A^-(\mathbf{u}, \mathbf{n}) = R\Lambda^- L,$$

where L and R denote the $m \times m$ matrices of left and right eigenvectors of $A(\mathbf{u}, \mathbf{n})$, respectively, and $\Lambda^- = \operatorname{diag}(\min(\lambda_i, 0))$ the $m \times m$ diagonal matrix of the negative eigenvalues of $A(\mathbf{u}, \mathbf{n})$.

For notational convenience, we denote by Ω_T the set $(0, T] \times \Omega$, Γ_T the boundary of Ω_T, and div the divergence with respect to the variable $\mathbf{x} = (x_0, x_1, \ldots, x_d)$, where x_0 denotes time t. In addition, we introduce the flux function $\mathcal{F}(\mathbf{u}) = (\mathbf{f}_0(\mathbf{u}), \mathbf{f}_1(\mathbf{u}), \ldots, \mathbf{f}_d(\mathbf{u}))$, with $\mathbf{f}_0 = \mathbf{u}$. Thereby, we may write the system of conservation laws (2.1) in the following compact form: find $\mathbf{u} : \Omega_T \to \mathbb{R}^m$ such that

$$\operatorname{div} \mathcal{F}(\mathbf{u}) = 0 \quad \text{in } \Omega_T, \tag{2.5}$$

subject to the initial condition in (2.1) and appropriate boundary conditions, cf. (2.4), for example.

3. Discontinuous Galerkin method. We begin by introducing the necessary notation. Suppose that $\mathcal{T}_h$ is a (space–time) subdivision of Ω_T into open element domains κ such that $\bar{\Omega}_T = \cup_{\kappa\in\mathcal{T}_h}\bar{\kappa}$. Here, h denotes the piecewise constant mesh function defined by $h|_\kappa \equiv h_\kappa = \mathrm{diam}(\kappa)$ for all $\kappa \in \mathcal{T}_h$. Let us assume that the family of subdivisions $\mathcal{T}_h$ is shape regular and that each $\kappa \in \mathcal{T}_h$ is a smooth bijective image of a fixed reference element $\hat{\kappa}$, that is, $\kappa = F_\kappa(\hat{\kappa})$ for all $\kappa \in \mathcal{T}_h$. Examples of different element types used in practice are presented in [24]; here, we shall only consider the case when $\hat{\kappa}$ is either the open unit simplex or the open unit hypercube in $\mathbb{R}^{d+1}$. On the reference element $\hat{\kappa}$ we define spaces of polynomials of degree $p \geq 0$ as follows:

$$\mathcal{Q}_p = \mathrm{span}\left\{\hat{\mathbf{x}}^\alpha : 0 \leq \alpha_i \leq p,\ 0 \leq i \leq d\right\},$$
$$\mathcal{P}_p = \mathrm{span}\left\{\hat{\mathbf{x}}^\alpha : 0 \leq |\alpha| \leq p\right\}.$$

We now introduce the finite element space $S_{h,p}$ consisting of discontinuous vector–(of dimension m)–valued polynomial functions of degree $p \geq 0$, defined by

$$\begin{aligned} S_{h,p} = \{\mathbf{v} \in [L_2(\Omega_T)]^m : \mathbf{v}|_\kappa \circ F_\kappa \in [\mathcal{Q}_p]^m\,, \text{ if } \hat{\kappa} = F_\kappa^{-1}(\kappa) \text{ is the unit hypercube,}\\ \text{and } \mathbf{v}|_\kappa \circ F_\kappa \in [\mathcal{P}_p]^m\,, \text{ if } \hat{\kappa} = F_\kappa^{-1}(\kappa) \text{ is the unit simplex; } \kappa \in \mathcal{T}_h\}\ . \end{aligned}$$

For each $\kappa \in \mathcal{T}_h$ and any $v \in H^1(\kappa)$ we denote by v_κ^+ the interior trace of v on $\partial\kappa$ (the trace taken from within κ). Now consider an element κ; then for each $\mathbf{x} \in \partial\kappa\backslash\Gamma_T$ (with the exception of a set of d–dimensional measure zero) there exists a unique element $\kappa' \neq \kappa$, depending on the choice of $\mathbf{x}$, such that $\mathbf{x} \in \partial\kappa'\backslash\Gamma_T$. Now suppose that $v \in H^1(\kappa)$ for each $\kappa \in \mathcal{T}_h$. On $\partial\kappa\backslash\Gamma_T$, for some $\kappa \in \mathcal{T}_h$, we define the outer trace v_κ^- of v on $\partial\kappa\backslash\Gamma_T$ relative to κ as the inner trace $v_{\kappa'}^+$ relative to those elements κ' for which $\partial\kappa'\backslash\Gamma_T$ has intersection with $\partial\kappa\backslash\Gamma_T$ of positive d–dimensional measure.

Since below it will always be clear from the context which element κ in the subdivision $\mathcal{T}_h$ the quantities v_κ^+ and v_κ^- correspond to, for the sake of notational simplicity, we shall suppress the letter κ in the subscript and write, respectively, v^+ and v^- instead.

To formulate the discontinuous Galerkin method, we first introduce a weak formulation of (2.5). To this end, we multiply the conservation law (2.5) by an arbitrary smooth function $\mathbf{v}$ and integrate by parts over an element κ in the mesh $\mathcal{T}_h$; thereby, we get

$$-\int_\kappa \mathcal{F}(\mathbf{u}) \cdot \nabla\mathbf{v}\,\mathrm{d}\mathbf{x} + \int_{\partial\kappa} \mathcal{F}(\mathbf{u}^+) \cdot \mathbf{n}_\kappa\,\mathbf{v}^+\,\mathrm{d}s = 0, \tag{3.1}$$

where ∇ denotes the gradient operator with respect to the variable $\mathbf{x} = (x_0, x_1, \ldots, x_d)$ and $\mathbf{n}_\kappa$ the unit outward normal vector to $\partial\kappa$.

To discretise (3.1), we replace the analytical solution $\mathbf{u}$ by the Galerkin finite element approximation $\mathbf{u}_h$ and the test function $\mathbf{v}$ by $\mathbf{v}_h$, where $\mathbf{u}_h$ and $\mathbf{v}_h$ both belong to the finite element space $S_{h,p}$. In addition, since the numerical solution $\mathbf{u}_h$ is discontinuous between element interfaces, we must replace the flux $\mathcal{F}(\mathbf{u}^+)\cdot\mathbf{n}_\kappa$ by a *numerical flux* function $\mathcal{H}(\mathbf{u}_h^+, \mathbf{u}_h^-, \mathbf{n}_\kappa)$, which depends on both the inner– and outer–trace of $\mathbf{u}_h$ on $\partial\kappa$, $\kappa \in \mathcal{T}_h$, and the unit outward normal $\mathbf{n}_\kappa$ to $\partial\kappa$. Thereby, summing over the elements κ in the mesh $\mathcal{T}_h$, yields the discontinuous Galerkin finite element discretisation of (2.5) as follows: find $\mathbf{u}_h \in S_{h,p}$ such that

$$\sum_{\kappa\in\mathcal{T}_h} \left\{-\int_\kappa \mathcal{F}(\mathbf{u}_h) \cdot \nabla\mathbf{v}_h\,\mathrm{d}\mathbf{x} + \int_{\partial\kappa} \mathcal{H}(\mathbf{u}_h^+, \mathbf{u}_h^-, \mathbf{n}_\kappa)\,\mathbf{v}_h^+\,\mathrm{d}s\right\} = 0 \quad \forall \mathbf{v}_h \in S_{h,p}, \tag{3.2}$$

cf. [3, 9, 10, 11], for example. Here, for elements $\kappa \in \mathcal{T}_h$ whose boundary intersect that of the computational domain Ω_T, we replace $\mathbf{u}_h^-$ by appropriate boundary/initial conditions on the portion of $\partial\kappa$ for which $\partial\kappa \cap \Gamma_T \neq \emptyset$.

We remark that the replacement of the flux $\mathcal{F}(\mathbf{u}^+) \cdot \mathbf{n}_\kappa$ by the numerical flux function $\mathcal{H}(\mathbf{u}_h^+, \mathbf{u}_h^-, \mathbf{n}_\kappa)$ on the boundary of element κ, κ in $\mathcal{T}_h$, corresponds to the weak imposition of the boundary data, cf. [3, 22]. Furthermore, we emphasise that the choice of the numerical flux function is *independent* of the finite element space employed. Indeed, the numerical flux $\mathcal{H}(\cdot,\cdot,\cdot)$ may be chosen to be any two–point monotone Lipschitz function which satisfies the following two conditions:

(i) $\mathcal{H}(\cdot,\cdot,\cdot)|_{\partial\kappa}$ is consistent with the flux $\mathcal{F}(\cdot) \cdot \mathbf{n}_\kappa$ for each κ in $\mathcal{T}_h$; i.e.

$$\mathcal{H}(\mathbf{u}, \mathbf{u}, \mathbf{n}_\kappa)|_{\partial\kappa} = \mathcal{F}(\mathbf{u}) \cdot \mathbf{n}_\kappa \quad \forall \kappa \in \mathcal{T}_h;$$

(ii) $\mathcal{H}(\cdot,\cdot,\cdot)$ is conservative, i.e. given any two neighbouring elements κ and κ' from the finite element partition $\mathcal{T}_h$, at each point $\mathbf{x} \in \partial\kappa \cap \partial\kappa' \neq \emptyset$, noting that $\mathbf{n}_{\kappa'} = -\mathbf{n}_\kappa$, we have that

$$\mathcal{H}(\mathbf{v}, \mathbf{w}, \mathbf{n}_\kappa) = -\mathcal{H}(\mathbf{w}, \mathbf{v}, -\mathbf{n}_\kappa).$$

There are several numerical flux functions satisfying these conditions, such as the Godunov flux, the Engquist–Osher flux, the Lax–Friedrichs flux, the Roe flux and the Vijayasundaram flux, for example; cf. Kröner [26] and Toro [32], for example, and the references cited therein. In Section 7 we shall consider two different numerical fluxes; on triangular elements, we employ the (local) Lax–Friedrichs flux, while on quadrilateral elements, we implement the Vijayasundaram flux.

The (local) Lax–Friedrichs flux $\mathcal{H}_{LF}(\cdot,\cdot,\cdot)$, is defined by

$$\mathcal{H}_{LF}(\mathbf{u}_h^+, \mathbf{u}_h^-, \mathbf{n}_\kappa)|_{\partial\kappa} = \frac{1}{2}\left(\mathcal{F}(\mathbf{u}_h^+) \cdot \mathbf{n}_\kappa + \mathcal{F}(\mathbf{u}_h^-) \cdot \mathbf{n}_\kappa - \alpha\left(\mathbf{u}_h^- - \mathbf{u}_h^+\right)\right) \quad \text{for } \kappa \in \mathcal{T}_h,$$

where α is an estimate of the largest eigenvalue (in absolute value) of the Jacobi matrix

$$\mathcal{A}(\mathbf{u}_h, \mathbf{n}_\kappa) = \frac{\partial}{\partial \mathbf{u}}\mathcal{F}(\mathbf{u}_h) \cdot \mathbf{n}_\kappa \equiv \sum_{i=0}^{d} A_i(\mathbf{u}_h)\,(\mathbf{n}_\kappa)_i\,,$$

in the neighbourhood of the boundary $\partial\kappa$. Here, A_i, $i = 0, \ldots, d$, are the Jacobi matrices defined in (2.2); note that for $i = 0$, $\mathbf{f}_0 = \mathbf{u}$, and thus A_0 is the identity matrix. Furthermore, $(\mathbf{n}_\kappa)_i$ denotes the ith component of the unit outward normal vector $\mathbf{n}_\kappa$ to element κ, $\kappa \in \mathcal{T}_h$, for $i = 0, \ldots, d$.

The Vijayasundaram flux $\mathcal{H}_V(\cdot,\cdot,\cdot)$, is defined by

$$\mathcal{H}_V(\mathbf{u}_h^+, \mathbf{u}_h^-, \mathbf{n}_\kappa)|_{\partial\kappa} = \mathcal{A}^+(\hat{\mathbf{u}}_h, \mathbf{n}_\kappa)\mathbf{u}_h^+ + \mathcal{A}^-(\hat{\mathbf{u}}_h, \mathbf{n}_\kappa)\mathbf{u}_h^- \quad \text{for } \kappa \in \mathcal{T}_h,$$

where $\mathcal{A}^+(\hat{\mathbf{u}}_h, \mathbf{n}_\kappa)$ and $\mathcal{A}^-(\hat{\mathbf{u}}_h, \mathbf{n}_\kappa)$ denote the positive and negative parts of the Jacobi matrix $\mathcal{A}(\hat{\mathbf{u}}_h, \mathbf{n}_\kappa)$, respectively, evaluated at some average state $\hat{\mathbf{u}}_h$ between $\mathbf{u}_h^+$ and $\mathbf{u}_h^-$.

Finally, we remark that even when the fluxes at inter-element boundaries are upwinded through the choice of an appropriate numerical flux function $\mathcal{H}(\cdot,\cdot,\cdot)$, spurious oscillations may still be generated by the discontinuous Galerkin finite element method (3.2), in the vicinity of sharp features of the analytical solution, when higher–order degree polynomials are used; i.e. when $p > 0$. In order to compute physically relevant solutions which do not exhibit such oscillatory behaviour, the basic discontinuous Galerkin scheme (3.2) must be enhanced by the addition of some form of nonlinear dissipation mechanism which does not adversely affect the formal order of accuracy of the scheme. Indeed, much research activity has focused on the development of appropriate stabilisation devices; for example, Cockburn *et al.* [9, 11] have proposed the use of local projection/limiting techniques for the Runge–Kutta discontinuous Galerkin finite element method, see also Biswas *et al.* [5]. Giannakouros & Karniadakis have considered the implementation of the flux corrected transport algorithm for spectral element approximations of nonlinear hyperbolic problems, cf. [14], for example. For a review of these and other techniques, we refer to Gottlieb & Hesthaven [15].

The *a posteriori* error analysis presented in the proceeding section is based on a hyperbolic duality argument employing the so–called Galerkin orthogonality property of the finite element method, cf. (3.7) below. Thereby, any stabilisation technique used to enhance the numerical performance of the standard discontinuous Galerkin method (3.2) should not violate this orthogonality condition. To this end, we add an artificial viscosity term (also referred to as a 'shock–capturing' term) to the scheme (3.2) which depends on both the mesh function h and the finite element residual. The dependence of the shock–capturing term on the residual of the underlying conservation law ensures the consistency of the resulting finite element method for smooth analytical solutions $\mathbf{u}$. We note that this shock–capturing term is isotropic; i.e. it includes both diffusion in the direction of the streamlines, as well as cross–wind diffusion. This is in contrast to the so–called streamline–diffusion method, cf. [16], for example, which modifies the test function $\mathbf{v}_h$ appearing in (3.2) to give least–squares control of the finite element residual; this has the effect of only adding artificial diffusion in the streamwise direction.

Thereby, we now consider the following discontinuous Galerkin finite element discretisation of (2.5): find $\mathbf{u}_h \in S_{h,p}$ such that

$$\sum_{\kappa\in\mathcal{T}_h}\left\{-\int_\kappa \mathcal{F}(\mathbf{u}_h)\cdot\nabla\mathbf{v}_h\,\mathrm{d}\mathbf{x} + \int_{\partial\kappa}\mathcal{H}(\mathbf{u}_h^+,\mathbf{u}_h^-,\mathbf{n}_\kappa)\,\mathbf{v}_h^+\,\mathrm{d}s \right.$$
$$\left. + \int_\kappa \varepsilon\nabla\mathbf{u}_h\cdot\nabla\mathbf{v}_h\,\mathrm{d}\mathbf{x}\right\} = 0 \quad \forall \mathbf{v}_h\in S_{h,p}. \tag{3.3}$$

Here, ε denotes the artificial viscosity coefficient matrix defined by

$$\varepsilon = C_\varepsilon\, h^{2-\beta}\,|\mathrm{div}\mathcal{F}(\mathbf{u}_h)|\, I_d, \tag{3.4}$$

where C_ε and $0<\beta<1/2$ are positive constants and $I_d = \mathrm{diag}(0,1,\ldots,1)$. The definition of ε in (3.4) represents a slight modification of the artificial viscosity model introduced and analysed by Jaffre *et al.* [24]; here, we have simplified the definition of ε to only include the *interior* residual term $|\mathrm{div}\mathcal{F}(\mathbf{u}_h)|$, cf. (4.9). We note that in [24], the discontinuous Galerkin finite element method (3.3), with the addition of streamline–diffusion stabilisation and the numerical flux function $\mathcal{H}(\cdot,\cdot,\cdot)$ defined as the (global) Lax–Friedrichs flux, was shown to be convergent for any approximating polynomial of degree $p\geq 0$ on general meshes for multidimensional scalar problems, and entropy consistent for multidimensional systems.

REMARK 3.1. *The addition of the artificial viscosity term with coefficient matrix ε introduces two parameters into the resulting discontinuous Galerkin scheme; namely, C_ε and β. An automatic procedure for determining the correct level of artificial viscosity to be added into the scheme would obviously be advantageous. We note that in the* *context of streamline–diffusion stabilisation, work has been conducted in [6, 13, 19], for example, to automatically determine the size of the streamline–diffusion parameter, thereby rendering the method free of any numerical tuning. Extensions of these techniques to yield parameter–free shock capturing terms is possible; however, this is beyond the scope the current paper and will be considered elsewhere.*

Introducing the semi-linear form $\mathcal{N}(\cdot,\cdot)$ that is nonlinear in its first argument and linear in its second, we may write the discontinuous Galerkin finite element method (3.3) in the following compact form: find $\mathbf{u}_h \in S_{h,p}$ such that

$$\mathcal{N}(\mathbf{u}_h, \mathbf{v}_h) = 0 \quad \forall \mathbf{v}_h \in S_{h,p}. \tag{3.5}$$

Inserting the exact solution $\mathbf{u}$ into (3.5) and using both, the dependence of the shock-capturing term on the residual and the consistency condition of the numerical flux function $\mathcal{H}(\cdot,\cdot,\cdot)$, cf. condition (i) above, we deduce that if the analytical solution to (2.5) is sufficiently regular, then the following consistency condition holds:

$$\mathcal{N}(\mathbf{u}, \mathbf{v}_h) = 0 \quad \forall \mathbf{v}_h \in S_{h,p}. \tag{3.6}$$

Thereby, in the nonlinear case, the Galerkin orthogonality property of the finite element method (3.5) is expressed as follows:

$$\mathcal{N}(\mathbf{u}, \mathbf{v}_h) - \mathcal{N}(\mathbf{u}_h, \mathbf{v}_h) = 0 \quad \forall \mathbf{v}_h \in S_{h,p}. \tag{3.7}$$

4. A posteriori error analysis. In this section, we shall be interested in controlling the error of the numerical solution measured not only in terms of some global norm, but in terms of a given target functional $J(\cdot)$ (sometimes referred to as the error functional). Here, $J(\cdot)$ is the physical quantity of interest and may, for example, represent the mean flow across a line, a point value of the solution, or the lift or drag coefficients of a body immersed into an inviscid fluid.

The proceeding error analysis is based on a hyperbolic duality argument using the general approach developed by R. Rannacher and his collaborators, see [4, 17, 21, 28, 29], for example; see also [23, 30] for the application of these techniques to high–order hp–finite element approximations to first–order hyperbolic problems. We begin by first introducing some notation. Assuming that the functional of interest $J(\cdot)$ is differentiable, we write $\bar{J}(\cdot;\cdot)$ to denote the mean value linearisation of $J(\cdot)$ defined by

$$\bar{J}(\mathbf{u}, \mathbf{u}_h; \mathbf{u} - \mathbf{u}_h) = J(\mathbf{u}) - J(\mathbf{u}_h) = \int_0^1 J'[\theta\mathbf{u} + (1-\theta)\mathbf{u}_h](\mathbf{u} - \mathbf{u}_h)\,\mathrm{d}\theta, \tag{4.1}$$

where $J'[\mathbf{w}](\cdot)$ denotes the functional (Fréchet) derivative of $J(\cdot)$ evaluated at some $\mathbf{w}$ in V. Here, V is some suitably chosen function space such that $S_{h,p} \subset V$.

Analogously, we write $\mathcal{M}(\mathbf{u}, \mathbf{u}_h; \cdot, \cdot)$ to denote the mean–value linearisation of the semi–linear form $\mathcal{N}(\cdot,\cdot)$ given by

$$\begin{aligned} \mathcal{M}(\mathbf{u}, \mathbf{u}_h; \mathbf{u} - \mathbf{u}_h, \mathbf{v}) &= \mathcal{N}(\mathbf{u}, \mathbf{v}) - \mathcal{N}(\mathbf{u}_h, \mathbf{v}) \\ &= \int_0^1 \mathcal{N}'_{\mathbf{u}}[\theta\mathbf{u} + (1-\theta)\mathbf{u}_h](\mathbf{u} - \mathbf{u}_h, \mathbf{v})\,\mathrm{d}\theta \end{aligned} \tag{4.2}$$

for all $\mathbf{v}$ in V. Here, $\mathcal{N}'_{\mathbf{u}}[\mathbf{w}](\cdot, \mathbf{v})$ denotes the Fréchet derivative of $\mathbf{u} \to \mathcal{N}(\mathbf{u}, \mathbf{v})$, for $\mathbf{v} \in V$ fixed, at some $\mathbf{w}$ in V. We remark that the linearisation defined in equation

(4.2) is only a *formal* calculation, in the sense that $\mathcal{N}'_{\mathbf{u}}[\mathbf{w}](\cdot,\mathbf{v})$ may not in general exist. Instead, a suitable approximation to $\mathcal{N}'_{\mathbf{u}}[\mathbf{w}](\cdot,\mathbf{v})$ in the direction $\mathbf{u}-\mathbf{u}_h$ must be determined, for example, by computing appropriate finite difference quotients of $\mathcal{N}(\cdot,\mathbf{v})$. Below we provide some concrete examples when $\mathcal{N}'_{\mathbf{u}}[\mathbf{w}](\cdot,\mathbf{v})$ may be uniquely determined; further discussion concerning the calculation of the Fréchet derivative of $\mathcal{N}(\cdot,\mathbf{v})$ with respect to $\mathbf{u}$, $\mathbf{v}\in V$ fixed, will be presented in Section 5.

For the purposes of the proceeding analysis, we *assume* that the linearisation performed in (4.2) is well–defined. Under this hypothesis, we introduce the following *dual* or *adjoint* problem: find $\mathbf{z}\in V$ such that

$$\mathcal{M}(\mathbf{u},\mathbf{u}_h;\mathbf{w},\mathbf{z}) = \bar{J}(\mathbf{u},\mathbf{u}_h;\mathbf{w}) \quad \forall \mathbf{w}\in V. \tag{4.3}$$

We assume that (4.3) possesses a unique solution. Clearly, the validity of this assumption depends on both the definition of $\mathcal{M}(\mathbf{u},\mathbf{u}_h;\cdot,\cdot)$ and the choice of the linear functional under consideration. Below, we present some important examples which are covered by our hypothesis.

Example 1: Linear hyperbolic problems. Let us first consider the case of a linear hyperbolic equation for the scalar ($m=1$) variable $\mathbf{u}\equiv u$; then we may write the flux function $\mathcal{F}(u)=\mathbf{a}u$, where $\mathbf{a}=(1,a_1,\ldots,a_d)$ and $a_i=a_i(\mathbf{x})$, for $i=1,\ldots,d$. The weak imposition of boundary conditions on each element gives rise to the following numerical flux function

$$\mathcal{H}(u_h^+,u_h^-,\mathbf{n}_\kappa)|_{\partial\kappa} = \mathbf{a}\cdot\mathbf{n}_\kappa \lim_{s\to 0^+} u_h(\mathbf{x}-s\mathbf{a}) \quad \text{for } \kappa\in\mathcal{T}_h,$$

cf. Cockburn *et al.* [10]. In the absence of shock–capturing, i.e. when $\varepsilon\equiv 0$, a simple calculation based on the divergence theorem shows that the dual solution z satisfies the (formal) adjoint equation subject to appropriate data, depending on the choice of the functional $J(\cdot)$. In particular, it was shown in [23] that if $J(\cdot)$ is chosen to represent the mean flow over Ω_T, the value of the solution at a given point $\mathbf{x}_c$ in Ω_T, or the normal flux along a portion of the outflow boundary of Γ_T, then the dual problem is indeed well–posed. Analogous well–posedness results for the dual problem also hold for systems of linear hyperbolic conservation laws provided the numerical flux function is chosen appropriately.

Example 2: Continuous Galerkin approximations to one–dimensional scalar hyperbolic problems. The question of well–posedness of the dual problem associated with nonlinear hyperbolic conservation laws is rather more delicate. Let us, for example, consider the following one–dimensional scalar hyperbolic equation

$$\frac{\partial}{\partial t}u(x,t)+\frac{\partial}{\partial x}f(u(x,t))=0, \quad -\infty<x<\infty, \quad 0<t\le T, \tag{4.4}$$

with strictly convex flux function f, i.e. $f''>0$, subject to the initial condition

$$u(x,0)=u_0(x), \quad -\infty<x<\infty. \tag{4.5}$$

Here, we suppose that (4.4), (4.5) is approximated by the standard Galerkin finite element method consisting of continuous piecewise polynomials in both space and time, cf. [29]. Furthermore, we suppose that the functional of interest represents the (weighted) mean flow in space; i.e.

$$J(w)\equiv M_\psi(w)=\int_{-\infty}^{\infty} w\psi\,\mathrm{d}x,$$

where $\psi \in L_2(-\infty,\infty)$ is a given weight function. According to (4.3), the dual problem (in strong form) takes the following form: find z such that

$$
\begin{aligned}
-\frac{\partial z}{\partial t} - a(x,t)\frac{\partial z}{\partial x} &= 0, \qquad -\infty < x < \infty, \quad 0 \le t < T, \\
z(x,T) &= \psi(x), \qquad -\infty < x < \infty,
\end{aligned}
\tag{4.6}
$$

where

$$
a(x,t) = \int_0^1 f'((1-\theta)u + \theta u_h)\,\mathrm{d}\theta.
$$

Although the dual problem (4.6) is linear, this is a non-standard hyperbolic problem since the spatial velocity field a may be discontinuous. Thereby, in this case the standard classical theory of well–posedness of linear hyperbolic equations does not apply. However, assuming that $a \in L_\infty(\mathbb{R}\times(0,T))$ and satisfies a one–sided Lipschitz condition, Tadmor [31] has shown that (4.6) is a meaningful problem. For further details, and the verification that a satisfies the desired hypotheses when f is strictly convex, we refer to Süli [29].

In general, however, it is not known whether the dual problem (4.3) possesses a unique solution when the hyperbolic conservation law (2.5) is nonlinear, and when the discontinuous Galerkin approximation (3.3) is employed, even for scalar problems, corresponding to $m = 1$. We can only *hypothesise* that the computation of a physically correct approximation to (2.5) will yield a uniquely solvable dual problem. In the absence of such analytical results, we must rely solely on numerical simulation to confirm the validity of this hypothesis. Indeed, in Section 7, we consider a series of test problems which provide numerical evidence to indicate that the dual problem is solvable for the particular target functionals selected.

For the proceeding error analysis, we must therefore *assume* that the dual problem (4.3) is well–posed. Under this assumption, we have the following general result.

THEOREM 4.1. *Let $\mathbf{u}$ and $\mathbf{u}_h$ denote the solutions of (2.5) and (3.3), respectively, and suppose that the dual problem (4.3) is well–posed. Then, the following error representation formula holds:*

$$
J(\mathbf{u}) - J(\mathbf{u}_h) = \mathcal{E}_\Omega(\mathbf{u},\mathbf{u}_h,h,\mathbf{z}-\mathbf{z}_h) \equiv \sum_{\kappa\in\mathcal{T}_h} \eta_\kappa,
\tag{4.7}
$$

where

$$
\eta_\kappa = \int_\kappa R_h\,(\mathbf{z}-\mathbf{z}_h)\,d\mathbf{x} + \int_{\partial\kappa} r_h\,(\mathbf{z}-\mathbf{z}_h)^+\,ds - \int_\kappa \varepsilon\nabla\mathbf{u}_h\cdot\nabla(\mathbf{z}-\mathbf{z}_h)\,d\mathbf{x}
\tag{4.8}
$$

for all $\mathbf{z}_h$ in $S_{h,p}$. Here, R_h and r_h denote the internal and boundary finite element residuals, respectively, defined on $\kappa\in\mathcal{T}_h$ by

$$
R_h|_\kappa = -div\mathcal{F}(\mathbf{u}_h) \quad and \quad r_h|_\kappa = \mathcal{F}(\mathbf{u}_h^+)\cdot\mathbf{n}_\kappa - \mathcal{H}(\mathbf{u}_h^+,\mathbf{u}_h^-,\mathbf{n}_\kappa),
\tag{4.9}
$$

respectively.

Proof. Choosing $\mathbf{w} = \mathbf{u}-\mathbf{u}_h$ in (4.3), recalling the linearisation performed in (4.1), and exploiting the Galerkin orthogonality property (3.7), we get

$$
\begin{aligned}
J(\mathbf{u}) - J(\mathbf{u}_h) &= \bar{J}(\mathbf{u},\mathbf{u}_h;\mathbf{u}-\mathbf{u}_h) \\
&= \mathcal{M}(\mathbf{u},\mathbf{u}_h;\mathbf{u}-\mathbf{u}_h,\mathbf{z}) \\
&= \mathcal{M}(\mathbf{u},\mathbf{u}_h;\mathbf{u}-\mathbf{u}_h,\mathbf{z}-\mathbf{z}_h) \\
&= -\mathcal{N}(\mathbf{u}_h,\mathbf{z}-\mathbf{z}_h)
\end{aligned}
$$

for all $\mathbf{z}_h$ in the finite element space $S_{h,p}$. By employing the divergence theorem, we deduce that

$$
\begin{aligned}
J(\mathbf{u}) - J(\mathbf{u}_h) = \sum_{\kappa\in\mathcal{T}_h} \Big\{ & - \int_\kappa \mathrm{div}\mathcal{F}(\mathbf{u}_h)(\mathbf{z}-\mathbf{z}_h)\,\mathrm{d}\mathbf{x} \\
& + \int_{\partial\kappa} \left(\mathcal{F}(\mathbf{u}_h^+)\cdot\mathbf{n}_\kappa - \mathcal{H}(\mathbf{u}_h^+,\mathbf{u}_h^-,\mathbf{n}_\kappa)\right)(\mathbf{z}-\mathbf{z}_h)^+\,\mathrm{d}s \\
& - \int_\kappa \varepsilon\nabla\mathbf{u}_h\cdot\nabla(\mathbf{z}-\mathbf{z}_h)\,\mathrm{d}\mathbf{x} \Big\}. \qquad (4.10)
\end{aligned}
$$

Using the definition of the internal and boundary residuals in (4.9), gives the desired result. □

Based on the general error representation formula derived in Theorem 4.1, *a posteriori* error estimates bounding the error in the computed functional $J(\cdot)$ may be deduced. Before we proceed, let us first recall the classification of Type I and Type II *a posteriori* error bounds introduced in [23]. Type I *a posteriori* error bounds, also referred to as *weighted a posteriori* error bounds (cf. Rannacher [28], for example), involve the multiplication of the residual terms R_h and r_h and the shock capturing term $\varepsilon\nabla\mathbf{u}_h$, by the difference between the dual solution $\mathbf{z}$ and its projection, interpolant or quasi-interpolant $\mathbf{z}_h$. On the other hand, Type II *a posteriori* bounds are in the spirit of the error estimates derived by C. Johnson *et al.* [12], and do not depend explicitly on the dual solution. These latter error estimates are derived from Type I *a posteriori* bounds by employing standard results from approximation theory, together with well–posedness results for the dual problem. The resulting Type II error bounds only involve certain norms of the residuals and shock–capturing term, the mesh function h, interpolation constants and the stability factor of the dual problem.

However, as we shall see in Section 7, the elimination of the 'weighting terms' involving the difference between $\mathbf{z}$ and $\mathbf{z}_h$ may adversely affect the performance of our adaptive finite element method. Indeed, mesh refinement strategies based on Type II *a posteriori* error bounds which do not require the computation of the dual solution may, under mesh refinement, lead to suboptimal convergence of the error $|J(\mathbf{u}) - J(\mathbf{u}_h)|$ in the computed functional, resulting in uneconomical mesh design and an inefficient adaptive algorithm (see [17, 21], for related work). For this reason, we only consider the derivation of the following Type I *a posteriori* error bound.

COROLLARY 4.2. *Under the assumptions of Theorem 4.1, the following Type I* a posteriori *error bound holds:*

$$
|J(\mathbf{u}) - J(\mathbf{u}_h)| \le \mathcal{E}_{|\Omega|}(\mathbf{u},\mathbf{u}_h,h,\mathbf{z}-\mathbf{z}_h) \equiv \sum_{\kappa\in\mathcal{T}_h} |\eta_\kappa|, \qquad (4.11)
$$

where η_κ is defined as in (4.8).

Proof. The *a posteriori* error bound (4.11) follows trivially from (4.7) by application of the triangle inequality. □

We end this section by noting that for nonlinear hyperbolic conservation laws and/or nonlinear target functionals $J(\cdot)$, both the error representation formula (4.7) and the resulting Type I *a posteriori* error bound (4.11) depend on the unknown analytical solution to both the primal and dual problems, $\mathbf{u}$ and $\mathbf{z}$, respectively. Thus, in order to render these error estimates computable, both $\mathbf{u}$ and $\mathbf{z}$ must be replaced by suitable approximations which do not adversely affect the reliability of the Type I *a posteriori* error bound (4.11), in the sense that the right–hand side of (4.11) does not under estimate the true error in the computed functional $J(\cdot)$. This subject will be the topic of the following section.

5. Numerical approximation of the dual problem. To ensure that the error representation formula proved in Theorem 4.1 and the subsequent error bound derived in Corollary 4.2 are genuinely *a posteriori*, all non-computable quantities appearing in the right–hand side of (4.7) and (4.11), respectively, must be replaced by suitable approximations; namely, the analytical solution to the primal problem $\mathbf{u}$, and the analytical solution to the dual problem $\mathbf{z}$.

Let us first deal with the approximation of $\mathbf{u}$. To this end, we note that the dependence of the error representation formula $\mathcal{E}_\Omega$ and the *a posteriori* error bound $\mathcal{E}_{|\Omega|}$ on $\mathbf{u}$ stems from the mean value linearisation of $\mathcal{N}(\cdot,\mathbf{v})$, $\mathbf{v} \in V$ fixed, and $J(\cdot)$ carried out in (4.2) and (4.1), respectively. Hence, for linear hyperbolic conservation laws and linear target functionals $J(\cdot)$, the dependence of the error representation formula (4.7) and the *a posteriori* error bound (4.11) on $\mathbf{u}$ does not arise. In practice, for nonlinear problems and/or nonlinear target functionals, the linearisation leading to $\mathcal{M}(\mathbf{u},\mathbf{u}_h;\cdot,\cdot)$ and $\bar{J}(\mathbf{u},\mathbf{u}_h;\cdot)$ is performed about the numerical solution $\mathbf{u}_h$, rather than at some convex combination of $\mathbf{u}$ and $\mathbf{u}_h$; i.e. $\mathcal{M}(\mathbf{u},\mathbf{u}_h;\cdot,\cdot)$ is approximated by $\mathcal{M}(\mathbf{u}_h,\mathbf{u}_h;\cdot,\cdot)$ in (4.2) and $\bar{J}(\mathbf{u},\mathbf{u}_h;\cdot)$ is approximated by $\bar{J}(\mathbf{u}_h,\mathbf{u}_h;\cdot)$ in (4.1), cf. [28], for example.

Secondly, the dual problem must be numerically approximated; here, there are essentially two further sources of error introduced into the computation of $\mathcal{E}_\Omega$ and $\mathcal{E}_{|\Omega|}$. Firstly, since the formal calculation of the Fréchet derivative of $\mathbf{u} \to \mathcal{N}(\mathbf{u},\mathbf{v})$, for $\mathbf{v} \in V$ fixed, at some $\mathbf{w}$ in V may not in general exist, the directional derivative $\mathcal{N}'_{\mathbf{u}}[\mathbf{w}](\mathbf{u}-\mathbf{u}_h,\mathbf{v})$, must be approximated by taking suitably defined finite difference quotients of $\mathcal{N}(\cdot,\mathbf{v})$. Denoting the approximate Fréchet derivative of $\mathcal{N}(\cdot,\mathbf{v})$, $\mathbf{v} \in V$ fixed, at some $\mathbf{w}$ in V, by $\hat{\mathcal{N}}'_{\mathbf{u}}[\mathbf{w}](\cdot,\mathbf{v})$, we define

$$\hat{\mathcal{M}}(\mathbf{u},\mathbf{u}_h;\mathbf{u}-\mathbf{u}_h,\mathbf{v}) = \int_0^1 \hat{\mathcal{N}}'_{\mathbf{u}}[\theta\mathbf{u}+(1-\theta)\mathbf{u}_h](\mathbf{u}-\mathbf{u}_h,\mathbf{v})\,\mathrm{d}\theta\,. \tag{5.1}$$

Calculating the linearisation performed in (5.1) at $\mathbf{u}_h$, rather than at a convex combination of $\mathbf{u}$ and $\mathbf{u}_h$ (cf. above), we now define the following (approximate) dual problem: find $\hat{\mathbf{z}} \in V$ such that

$$\hat{\mathcal{M}}(\mathbf{u}_h,\mathbf{u}_h;\mathbf{w},\hat{\mathbf{z}}) = \bar{J}(\mathbf{u}_h,\mathbf{u}_h;\mathbf{w}) \quad \forall \mathbf{w} \in V. \tag{5.2}$$

We recall from the previous section that there were open questions concerned with the existence and uniqueness of the formal dual problem defined in (4.3). Indeed, for general nonlinear systems of hyperbolic conservation laws, it is not at all clear whether (4.3) is well posed for a given target functional $J(\cdot)$. In practice, we are concerned about the well–posedness of the approximate dual problem (5.2). Given that the dual problem (5.2) serves only as an approximation to the true dual problem (4.3), further approximations may be made in the definition of (5.2) in order to ensure that the resulting system of partial differential equations is well–posed. For example, the approximate dual problem (5.2) may have additional artificial viscosity included in order to guarantee the existence and uniqueness of $\hat{\mathbf{z}}$. For the purposes of the current paper, this last approximation is not performed, since for the model problems considered here, the dual problem (5.2) was always found to be numerically solvable. Of course, for more complicated engineering problems, this may not be the case, and the additional regularisation provided by a 'tune–up' of an artificial viscosity term may be necessary.

Finally, we note that once a suitable approximate dual problem has been defined, its analytical solution $\hat{\mathbf{z}}$ must be numerically determined. Writing $\hat{\mathbf{z}}_{\hat{h}}$ to denote this approximation, we remark that $\hat{\mathbf{z}}_{\hat{h}}$ should not be calculated using the same finite element space $S_{h,p}$ employed for the primal problem; otherwise the resulting error representation formula would be identically zero. In practice, there are essentially three approaches to computing a numerical approximation $\hat{\mathbf{z}}_{\hat{h}}$ of $\hat{\mathbf{z}}$. The first approach is to keep the degree p of the approximating polynomial used to compute $\mathbf{u}_h$ fixed, but compute $\hat{\mathbf{z}}_{\hat{h}}$ on a sequence of dual finite element meshes $\hat{\mathcal{T}}_{\hat{h}}$ which, in general, differ from the "primal meshes" $\mathcal{T}_h$. Alternatively, $\hat{\mathbf{z}}_{\hat{h}}$ may be computed using piecewise discontinuous polynomials of degree $\hat{p}$, $\hat{p} > p$, on the same finite element mesh $\mathcal{T}_h$ employed for the primal problem. A variant of this second approach is to compute the approximate dual problem using the same mesh $\mathcal{T}_h$ and polynomial degree p employed for the primal problem and to patchwise extrapolate the resulting approximate dual solution $\hat{\mathbf{z}}_{\hat{h}} \in S_{h,p}$ to a dual solution $\hat{\mathbf{z}}_{\hat{h}} \in S_{2h,\hat{p}}$, $\hat{p} > p$. While this latter approach is the cheapest of the three methods, and is still capable of producing adaptively refined meshes specifically tailored to the selected target functional, the quality of the resulting approximate error representation formula may be poor. For the purposes of the current paper, we prefer the second approach due to its computational simplicity of implementation; i.e. $\hat{\mathbf{z}}_{\hat{h}} \equiv \hat{\mathbf{z}}_h \in S_{h,\hat{p}}$, with $\hat{p} > p$.

To summarise, in practice there are three sources of error in the computation of the error representation formula (4.7) and the Type I *a posteriori* error bound (4.11):

1. Linearisation error stemming from the replacement of $\mathbf{u}$ by $\mathbf{u}_h$ in (4.2) and (4.1);
2. Error created by the approximation of the Fréchet derivative of $\mathcal{N}(\cdot, \mathbf{v})$, $\mathbf{v} \in V$ fixed, in the direction $\mathbf{u} - \mathbf{u}_h$;
3. Error generated in the numerical approximation of the (approximate) dual problem.

Notwithstanding these approximations, we shall show through numerical experimentation in Section 7, the reliability of the Type I *a posteriori* error bound (4.11) is not compromised, in the sense that

$$\hat{\mathcal{E}}_{|\Omega|} \equiv \mathcal{E}_{|\Omega|}(\mathbf{u}_h, \mathbf{u}_h, h, \hat{\mathbf{z}}_h - \mathbf{z}_h) = \sum_{\kappa \in \mathcal{T}_h} |\hat{\eta}_\kappa|, \tag{5.3}$$

where $\hat{\eta}_\kappa$ is defined as in (4.8) with $\mathbf{z}$ replaced by $\hat{\mathbf{z}}_h$, remains an upper bound on the true error in the target functional $J(\cdot)$. In particular, we shall show that the ratio of the approximate error representation formula

$$\hat{\mathcal{E}}_\Omega \equiv \mathcal{E}_\Omega(\mathbf{u}_h, \mathbf{u}_h, h, \hat{\mathbf{z}}_h - \mathbf{z}_h) = \sum_{\kappa \in \mathcal{T}_h} \hat{\eta}_\kappa \tag{5.4}$$

and the true value $J(\mathbf{u}) - J(\mathbf{u}_h)$ is extremely close to one; see [17, 20, 21, 27], for related work.

REMARK 5.1. *In the error representation formula (4.7), the function $\mathbf{z}_h$ may be chosen to be any element from the finite element space $S_{h,p}$ employed to approximate the primal problem (2.5). Here, we select $\mathbf{z}_h$ to be the projection of the numerical approximation $\hat{\mathbf{z}}_h$ to the dual problem (5.2) onto the finite element space $S_{h,p}$. In the theory of* a posteriori *error estimation of continuous Galerkin finite element methods this choice is extremely important in order to obtain local error indicators $|\hat{\eta}_\kappa|$ which exhibit the optimal rate of convergence as the mesh is refined. However, for the discontinuous Galerkin method, this choice is less important, since discontinuous* *finite element schemes satisfy a Galerkin orthogonality property, cf. (3.7), both on a global and* local *level. Thereby, employing the local Galerkin orthogonality property, the error indicators $\hat{\eta}_\kappa$ become*

$$\hat{\eta}_\kappa = \int_\kappa R_h\,\hat{\mathbf{z}}_h\,d\mathbf{x} + \int_{\partial\kappa} r_h\,\hat{\mathbf{z}}_h^+\,ds - \int_\kappa \varepsilon\nabla\mathbf{u}_h\cdot\nabla\hat{\mathbf{z}}_h\,d\mathbf{x}; \tag{5.5}$$

i.e. they no longer depend on the choice of $\mathbf{z}_h$.

As a final note, we remark that even if the *a posteriori* error bound (4.11) should fail to remain an upper bound on the true error in the computed functional $J(\cdot)$, then the adaptive mesh refinement algorithm outlined in the following section still provides the necessary local information to ensure that economical meshes, specifically tailored to the approximation of the underlying functional $J(\cdot)$ of interest, are generated.

6. Adaptive mesh refinement. In this section we now consider the design of the corresponding adaptive algorithm to ensure both the reliable and efficient control of the discretisation error between the true value of the selected target functional $J(\mathbf{u})$ and the actual computed value $J(\mathbf{u}_h)$. To this end, we employ the (approximate) *a posteriori* error bound $\hat{\mathcal{E}}_{|\Omega|}$, cf. (5.3), to determine when the desired level of accuracy has been achieved. For example, suppose that the aim of the computation is to compute $J(\cdot)$ such that the error $|J(\mathbf{u}) - J(\mathbf{u}_h)|$ is less than some user–defined tolerance $\mathtt{TOL}$, i.e.

$$|J(\mathbf{u}) - J(\mathbf{u}_h)| \le \mathtt{TOL},$$

then, in practice we may enforce the stopping criterion

$$\hat{\mathcal{E}}_{|\Omega|} \le \mathtt{TOL}. \tag{6.1}$$

If the condition (6.1) is not satisfied on the current finite element mesh $\mathcal{T}_h$, then the elementwise terms $|\hat{\eta}_\kappa|$ are employed as local error indicators to guide mesh refinement and coarsening. The cycle of the adaptive mesh refinement may be outlined as follows:

1. Construct an initial mesh $\mathcal{T}_h$.
2. Compute the numerical approximation to the primal problem $\mathbf{u}_h \in S_{h,p}$ on the current mesh $\mathcal{T}_h$.
3. Compute the numerical approximation to the dual problem $\hat{\mathbf{z}}_h \in S_{h,\hat{p}}$ on the same mesh employed for the primal problem, with $\hat{p} > p$.
4. Evaluate the approximate *a posterioiri* error bound $\hat{\mathcal{E}}_{|\Omega|} = \sum_{\kappa\in\mathcal{T}_h}\hat{\eta}_\kappa$, cf. (5.3).
5. If $\hat{\mathcal{E}}_{|\Omega|} \le \mathtt{TOL}$, where $\mathtt{TOL}$ is a given tolerance, then STOP.
6. Otherwise, refine and coarsen a fixed fraction of the total number of elements according to the size of the local error indicators $|\hat{\eta}_\kappa|$ and generate a new mesh $\mathcal{T}_h$; GOTO 2.

The goal of the mesh refinement and coarsening is to equidistribute the local error indicators $|\hat{\eta}_\kappa|$. During each refinement and coarsening step a fixed fraction of the total number of cells are refined and coarsened. In the following section, we set the refinement and coarsening fractions to be 20% and 10%, respectively.

7. Numerical experiments. In this section we present some numerical examples to highlight the advantages of designing an adaptive finite element algorithm based on the weighted error indicators $|\hat{\eta}_\kappa|$ in comparison with traditional refinement

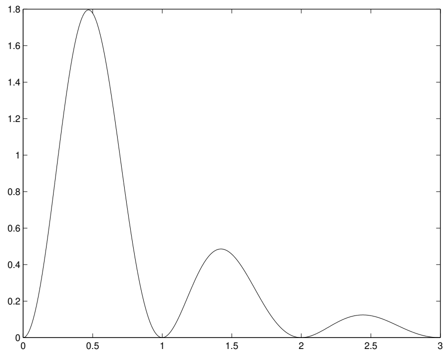

FIG. 7.1. *Example 1. Initial condition for Burgers' equation.*

strategies which do not require the solution of the dual problem (4.3). To this end, we consider the *ad hoc* error indicator

$$\eta_\kappa^{\mathrm{adhoc}} = \|hR_h\|_{L_2(\kappa)} + \|h^{1/2}r_h\|_{L_2(\partial\kappa)},$$

which stems from a Type II *a posteriori* error analysis, cf. [23].

In the following computations, both triangular and quadrilateral meshes will be employed; the latter are based on the deal.II library, cf. [1, 2]. Finally, we note that piecewise discontinuous (bi)linear functions are used to approximate the primal problem, i.e. $\mathbf{u}_h \in S_{h,1}$, and piecewise discontinuous (bi)quadratic functions to approximate the dual problem, i.e. $\hat{\mathbf{z}}_h \in S_{h,2}$.

7.1. Burgers' equation. In this first example we consider the one–dimensional unsteady inviscid Burgers' equation for the scalar variable $\mathbf{u} \equiv u$; i.e. we have

$$u_t + \left(\frac{1}{2}u^2\right)_x = 0, \tag{7.1}$$

on the space–time domain $\Omega_T = (0,2] \times (0,3)$, subject to the initial condition

$$\mathbf{u}(0,x) = \frac{2}{(1+x^3)}\,\sin^2(\pi x), \tag{7.2}$$

and boundary condition $u(t,0) = 0$ for $t \in [0,2]$, cf. Figure 7.1. The analytical solution to (7.1), (7.2) consists of three smooth 'hills' which form shock waves as time increases. These shocks will eventually merge to form a single line of discontinuity in the (t,x)–plane. Here, we only compute the numerical approximation up to a time after which the first two shock waves have merged, and select the functional of interest $J(\cdot)$ to be the value of the solution just before these two shocks interact with one another. More precisely, we choose

$$J(u) = u(1.35, 1.95);$$

thereby, the true value of the functional is $J(u) = 0.451408206331223$, cf. [30].

In Table 7.1, we demonstrate the performance of the adaptive algorithm with $C_\varepsilon = 1/4$ and $\beta = 1/10$. Here, we show the number of elements and degrees of freedom (DOF) in $S_{h,1}$, the true error in the functional $J(u) - J(u_h)$, the computed error representation formula (5.4), the approximate *a posteriori* error bound (5.3)

Elements	DOF	$J(u)-J(u_h)$	$\sum_\kappa \hat{\eta}_\kappa$	θ_1	$\sum_\kappa \lvert\hat{\eta}_\kappa\rvert$	θ_2
12	36	2.758e-02	-1.613e-01	-5.85	4.432e-01	16.07
25	75	1.574e-01	1.175e-01	0.75	2.751e-01	1.75
53	159	9.087e-02	-3.190e-02	-0.35	2.244e-01	2.47
110	330	6.231e-02	5.196e-02	0.83	1.206e-01	1.94
234	702	-1.566e-02	-3.274e-03	0.21	3.879e-02	2.48
479	1437	2.746e-04	3.301e-04	1.20	1.084e-02	39.48
1053	3159	1.281e-04	1.213e-04	0.95	3.273e-03	25.54
2256	6768	1.484e-05	1.458e-05	0.98	1.856e-03	125.06
4968	14904	-6.626e-07	-7.163e-07	1.08	7.762e-04	1171.38
11003	33009	-4.755e-07	-4.782e-07	1.01	3.196e-04	672.04
24662	73986	2.934e-08	2.905e-08	0.99	1.279e-04	4357.01

TABLE 7.1

Example 1. Adaptive algorithm for Burgers' equation.

and their respective effectivity indices θ_1 and θ_2. We see that initially on very coarse meshes the quality of the computed error representation formula $\hat{\mathcal{E}}_\Omega$ is very poor, in the sense that $\theta_1 = \hat{\mathcal{E}}_\Omega/(J(u) - J(u_h))$ is not close to one; however, as the mesh is refined the effectivity index θ_1 approaches unity. On the other hand, we observe that the Type I *a posteriori* error bound is not sharp, in the sense that the second effectivity index $\theta_2 = \hat{\mathcal{E}}_{|\Omega|}/|J(u)-J(u_h)|$ overestimates the true error in the computed functional by three orders of magnitude on the finest mesh; this loss of sharpness is attributed to the loss of inter–element cancellation of the local error indicators $\hat{\eta}_\kappa$, when the triangle inequality is employed. Thereby, it is clear that any further bounding performed *en route* to deriving a Type II *a posteriori* estimate will further adversely affect the quality of the computed error bound.

In Figure 7.2 we show the meshes generated using both the weighted error indicator $|\hat{\eta}_\kappa|$ and the *ad hoc* error indicator $\eta_\kappa^{\mathrm{adhoc}}$. From Figure 7.2(a), we see that there is virtually no refinement in the regions of the computational domain where the shocks are located when $|\hat{\eta}_\kappa|$ is employed. Indeed, most of the mesh refinement is concentrated in the neighbourhood upstream of the point of interest. This is due to the presence of the weighting terms involving the difference between the (approximated) dual solution $\hat{z}_h$ and z_h which multiply the computable residual terms involving the numerical solution u_h in the definition of the local error indicator $|\hat{\eta}_\kappa|$, cf. (4.8) with z replaced by $\hat{z}_h$. Indeed, from Figure 7.2(c), we see that the dual solution consists of a single 'spike' or delta function located at the point of interest which is carried backwards along the single characteristic passing through $(t,x) = (1.35, 1.95)$ to the inflow boundary at $t = 0$; the reduction in height of this spike is attributed to the numerical and artificial viscosity inherent in the scheme. In contrast, we see that when these weighting terms are neglected, then the mesh produced using the *ad hoc* error indicator is largely concentrated in the vicinity of the first two shock waves, with some refinement of the third shock. In Figure 7.3, we compare the true error in the computed functional $J(\cdot)$ using the two mesh refinement strategies. Here, we clearly observe the superiority of the weighted *a posteriori* error indicators; on the final mesh the true error in the linear functional is over four orders of magnitude smaller than $|J(u)-J(u_h)|$ computed on the sequence of meshes produced using $\eta_\kappa^{\mathrm{adhoc}}$. This clearly indicates that a good numerical resolution of the shocks in this example is irrelevant for the accurate approximation of the functional of interest.

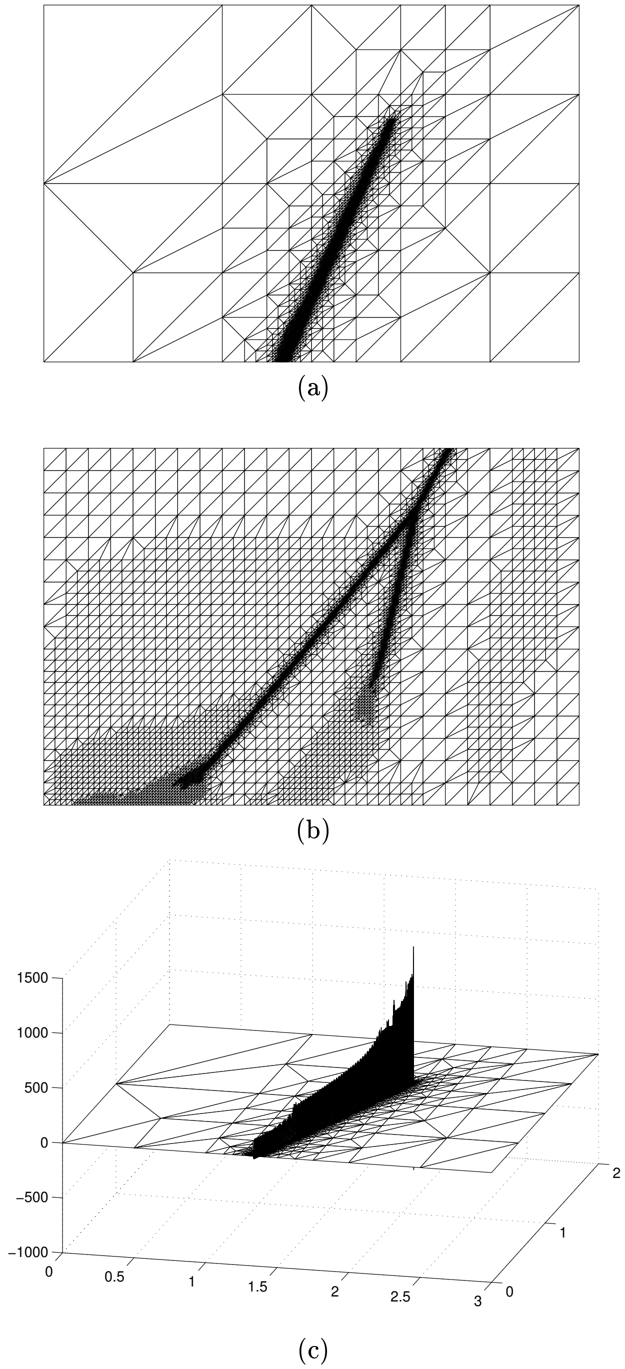

FIG. 7.2. *Example 1. (a) Mesh constructed using dual error indicator with* 24662 *elements and* 73986 *degrees of freedom* ($|J(u) - J(u_h)| = 2.934 \times 10^{-8}$)*; (b) Mesh constructed using* ad hoc *error indicator with* 20186 *elements and* 60558 *degrees of freedom* ($|J(u) - J(u_h)| = 4.015 \times 10^{-4}$)*; (c) Dual solution.*

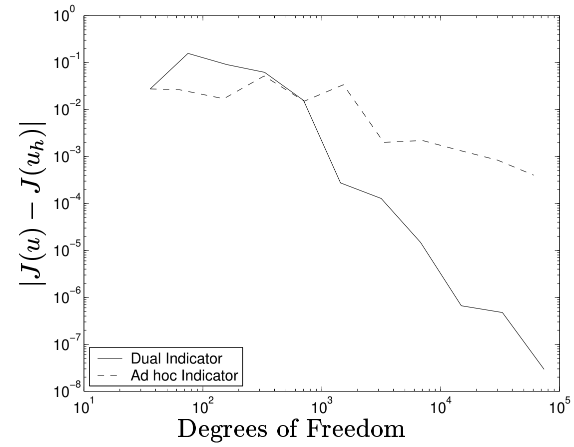

FIG. 7.3. *Example 1. Convergence of* $|J(u) - J(u_h)|$ *using the dual and* ad hoc *error indicators.*

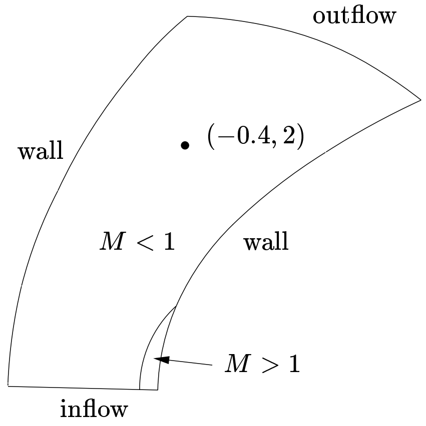

FIG. 7.4. *Example 2. Geometry for Ringleb's flow; here M denotes the Mach number.*

7.2. Ringleb's flow. In this second example we consider the steady two–dimensional compressible Euler equations; here, $\mathbf{u}$ represents the vector of conserved quantities $(\rho, \rho u, \rho v, \rho E)$, where ρ, (u, v) and E represent the density, Cartesian velocity and total energy per unit mass, respectively. Here, we consider Ringleb's flow for which an analytical solution may be obtained using the hodograph method, see Chiocchia [8] for details. This problem represents a transonic flow in a channel; the flow is mostly subsonic, with a small supersonic region near the right–hand side wall, cf. Figure 7.4.

We take the functional of interest to be the value of the density at the point $(-0.4, 2)$, i.e.,

$$J(\mathbf{u}) = \rho(-0.4, 2);$$

consequently the true value of the functional is given by $J(\mathbf{u}) = 0.8616065996968034$, cf. [30]. Given that the solution to Ringleb's flow is smooth, no artificial viscosity is required; thereby, we set $C_\varepsilon = 0$. In Table 7.2 we show the performance of our adaptive algorithm; here we see that the quality of the computed error representation formula is extremely good, with $\theta_1 \approx 1$ even on very coarse meshes. Furthermore,

Elements	DOF	$J(\mathbf{u})-J(\mathbf{u}_h)$	$\sum_\kappa \hat{\eta}_\kappa$	θ_1	$\sum_\kappa \lvert\hat{\eta}_\kappa\rvert$	θ_2
144	1728	-2.995e-04	-3.024e-04	1.01	2.914e-03	9.73
262	3144	8.839e-05	8.703e-05	0.98	1.239e-03	14.02
527	6324	2.937e-05	2.901e-05	0.99	3.793e-04	12.92
992	11904	5.083e-06	5.350e-06	1.05	2.863e-04	56.33
1785	21420	-3.274e-06	-3.225e-06	0.99	1.207e-04	36.87
3382	40584	-1.798e-06	-1.765e-06	0.98	4.274e-05	23.77
6337	76044	-8.327e-07	-8.293e-07	1.00	5.107e-05	61.34
11066	132792	-5.775e-07	-5.808e-07	1.01	1.829e-05	31.67
18924	227088	-2.827e-07	-2.833e-07	1.00	6.074e-06	21.49

TABLE 7.2
Example 2. Adaptive algorithm for Ringleb's flow.

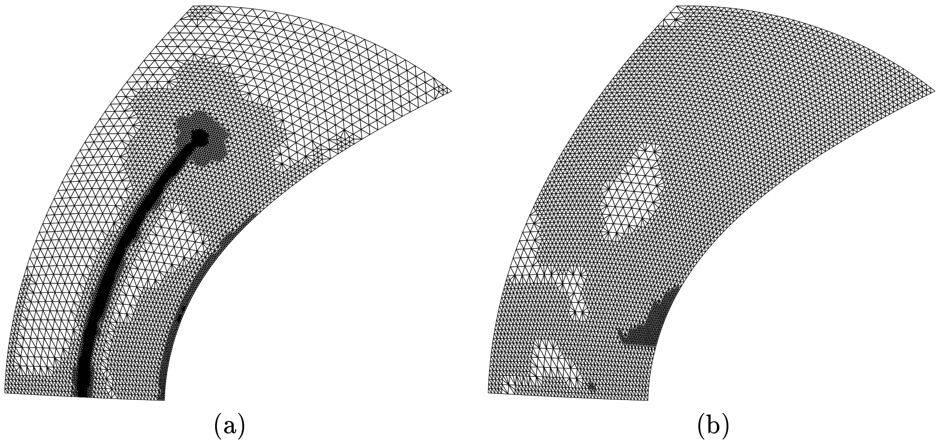

FIG. 7.5. *Example 2. (a) Mesh constructed using dual error indicator with* 18924 *elements and* 227088 *degrees of freedom* ($|J(\mathbf{u})-J(\mathbf{u}_h)| = 2.827\times 10^{-7}$); *(b) Mesh constructed using* ad hoc *error indicator with* 8965 *elements and* 107580 *degrees of freedom* ($|J(\mathbf{u})-J(\mathbf{u}_h)| = 7.238\times 10^{-6}$).

the Type I *a posteriori* error bound (4.11) is sharper for this smooth problem; here $\hat{\mathcal{E}}_{|\Omega|}$ overestimates the true error in the computed functional by about an order of magnitude.

The meshes produced using both our weighted error indicator $|\hat{\eta}_\kappa|$ and the *ad hoc* error indicator $\eta_\kappa^{\mathrm{adhoc}}$ are shown in Figure 7.5. Here, we see that, as in the previous example, the mesh constructed using $|\hat{\eta}_\kappa|$ is mostly concentrated in the neighbourhood upstream of the point of interest. However, due to the elliptic nature of the flow in the subsonic region, a circular region containing the point of interest is also refined, together with a strip of cells in the vicinity of the wall on the right–hand side of the domain enclosing the supersonic region of the flow. In Figure 7.6 we show the four components of the dual solution; for each component, we see that there is a spike centred at the point of interest which is transported towards the inflow boundary. We remark that these spikes 'diffuse out' slightly into the rest of the computational domain, thereby leading to the refinement of the mesh observed in Figure 7.5(a), when our weighted *a posteriori* error indicator is employed. In contrast, the mesh constructed using $\eta_\kappa^{\mathrm{adhoc}}$ is largely concentrated in the region near the right–hand wall, with further almost uniform refinement of the rest of the computational domain;

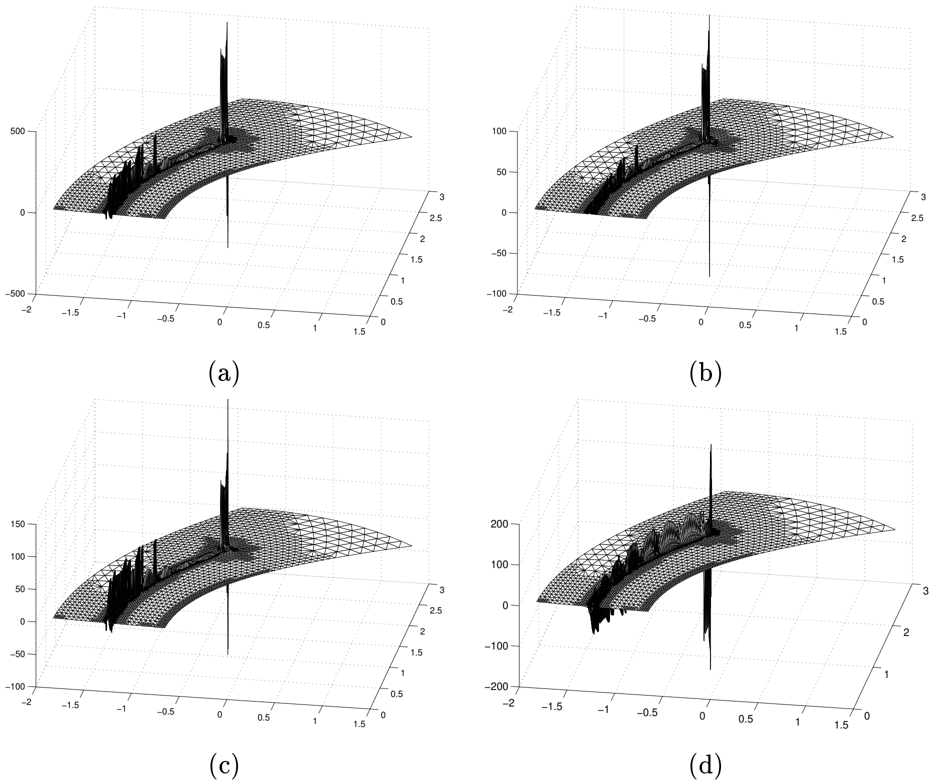

FIG. 7.6. *Example 2. Dual solution for Ringleb's flow: (a) z_1; (b) z_2; (c) z_3; (d) z_4.*

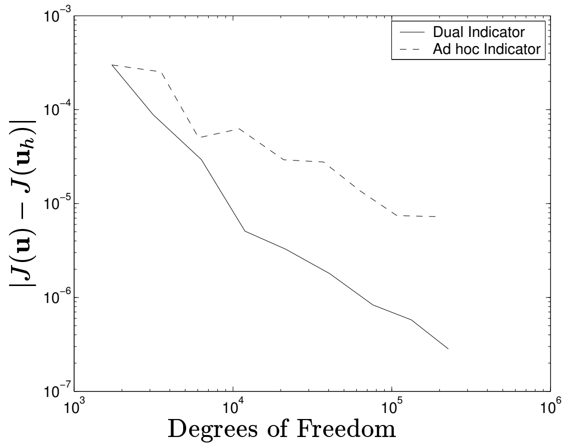

FIG. 7.7. *Example 2. Convergence of* $|J(\mathbf{u}) - J(\mathbf{u}_h)|$ *using the dual and* ad hoc *error indicators.*

we note that subsequent mesh refinement leads to an even greater concentration of elements near the wall. Finally, in Figure 7.7 we compare the true error in the computed functional $J(\cdot)$ using the two mesh refinement strategies. Again, as in the previous example, we clearly see that our weighted *a posteriori* error indicators produce more economical meshes than when the traditional *ad hoc* error indicator is

Elements	DOF	$J(\mathbf{u}) - J(\mathbf{u}_h)$	$\sum_\kappa \hat{\eta}_\kappa$	θ_1	$\sum_\kappa \|\hat{\eta}_\kappa\|$	θ_2
32	512	-6.946e-04	-8.609e-04	1.24	3.428e-03	4.94
56	896	9.940e-05	6.123e-05	0.62	1.619e-03	16.29
80	1280	-5.332e-05	-7.316e-05	1.37	9.163e-04	17.19
125	2000	7.571e-05	7.165e-05	0.95	5.488e-04	7.25
212	3392	-6.735e-06	-9.230e-06	1.37	2.412e-04	35.82
353	5648	1.634e-05	1.621e-05	0.99	1.096e-04	6.71
566	9056	5.681e-06	5.541e-06	0.98	5.141e-05	9.05
950	15200	2.778e-06	2.763e-06	0.99	2.001e-05	7.20
1562	24992	1.344e-06	1.367e-06	1.02	9.305e-06	6.92
2534	40544	1.750e-07	1.807e-07	1.03	4.463e-06	25.50

TABLE 7.3
Example 3. Adaptive algorithm for Ringleb's flow.

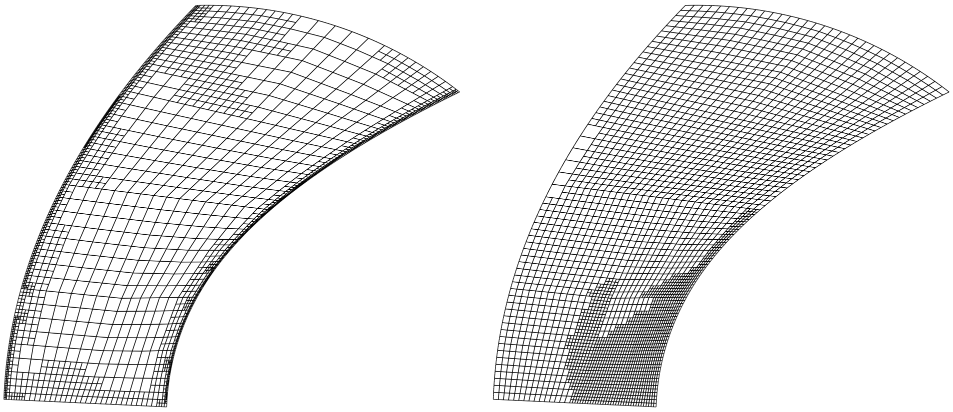

(a) (b)

FIG. 7.8. *Example 3. (a) Mesh constructed using dual error indicator with* 2534 *elements and* 40544 *degrees of freedom* ($|J(\mathbf{u}) - J(\mathbf{u}_h)| = 1.7504 \times 10^{-7}$); *(b) Mesh constructed using* ad hoc *error indicator with* 3056 *elements and* 48896 *degrees of freedom* ($|J(\mathbf{u}) - J(\mathbf{u}_h)| = 2.1622 \times 10^{-5}$).

employed, in the sense that $|J(\mathbf{u}) - J(\mathbf{u}_h)|$ is smaller for a given number of degrees of freedom. Indeed, on the final mesh the true error in the computed functional is over an order of magnitude smaller when the former error indicator is used.

7.3. Ringleb's flow (revisited). In this section, we again consider Ringleb's flow; here, we select the target functional to be the horizontal force component exerted on the channel walls. More precisely, we choose

$$J(\mathbf{u}) = \int_{\text{wall}} (\psi \cdot \mathbf{n}) p \, \mathrm{d}s,$$

where $\psi = (1, 0)$, $\mathbf{n}$ denotes the unit outward normal vector to the boundary and p is the pressure; this is a slight variant of the target functional selected in [27]. In this case, the true value of the functional on the exact geometry is given by $J(\mathbf{u}) = -0.574441759095$. We note that since the pressure p is derived from the conserved variables $(\rho, \rho u, \rho v, \rho E)$ using the equation of state (2.3), the selected target functional $J(\cdot)$ is nonlinear.

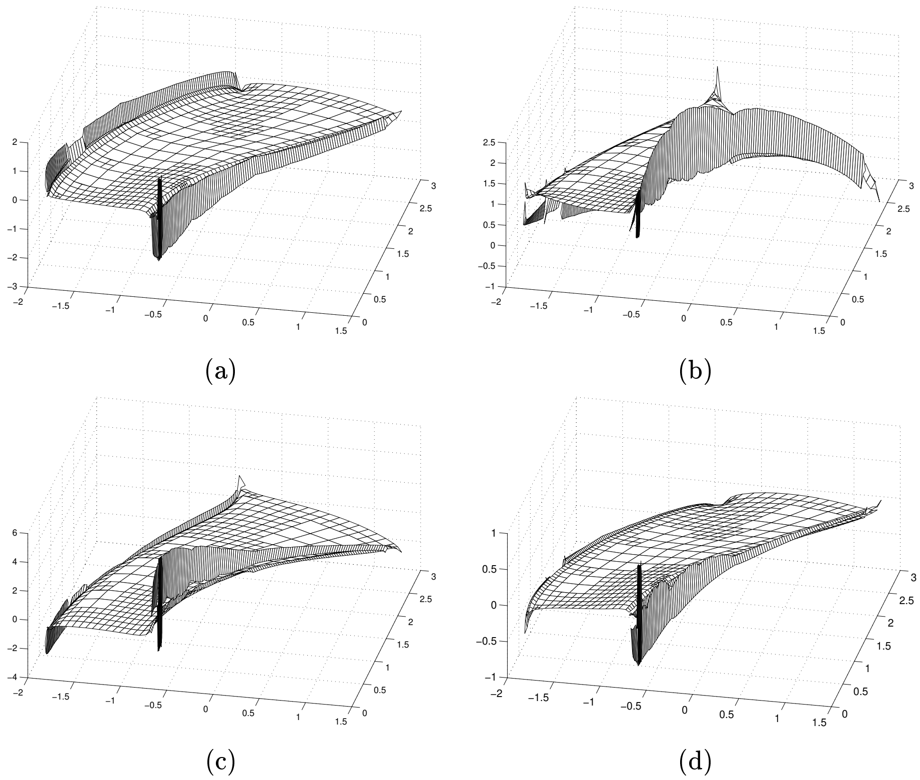

FIG. 7.9. *Example 3. Dual solution for Ringleb's flow: (a)* z_1*; (b)* z_2*; (c)* z_3*; (d)* z_4*.*

In Table 7.3 we show the performance of our adaptive algorithm; on each refinement level the computed value of the target functional $J(\mathbf{u}_h)$ is compared with the true value evaluated on the underlying computational domain. Here, we again see that the quality of the computed error representation formula is extremely good, with $\theta_1 \approx 1$, while the Type I *a posteriori* error bound overestimates the true error in the computed functional by about an order of magnitude. Figure 7.8 shows the meshes produced using both our weighted error indicator $|\hat{\eta}_\kappa|$ and the *ad hoc* error indicator $\eta_\kappa^{\text{adhoc}}$. Here, we observe that while the underlying (primal) problem has remained the same, the different choice of target functional selected leads to a different dual solution and hence to a completely different mesh when the error indicator $|\hat{\eta}_\kappa|$ is employed. Indeed in Figure 7.9, we now see that the four components of the dual solution are large in the vicinity of the solid channel walls; thereby this leads to the mesh being concentrated near the walls of the channel. In contrast, the *ad hoc* error indicator has no information concerning the target functional of interest, and will produce the same mesh irrespective of the choice of $J(\cdot)$; the corresponding mesh employing quadrilateral elements is similar in character to the one produced with triangular elements before, cf. Figure 7.5(b).

Finally, in Figure 7.10(a) we compare the true error in the computed functional $J(\cdot)$ using the two mesh refinement strategies. Again, as before, we clearly see that our weighted *a posteriori* error indicator produces more economical meshes than when the traditional *ad hoc* error indicator is employed; on the final mesh the true error in the computed functional is over two orders of magnitude smaller when the former error

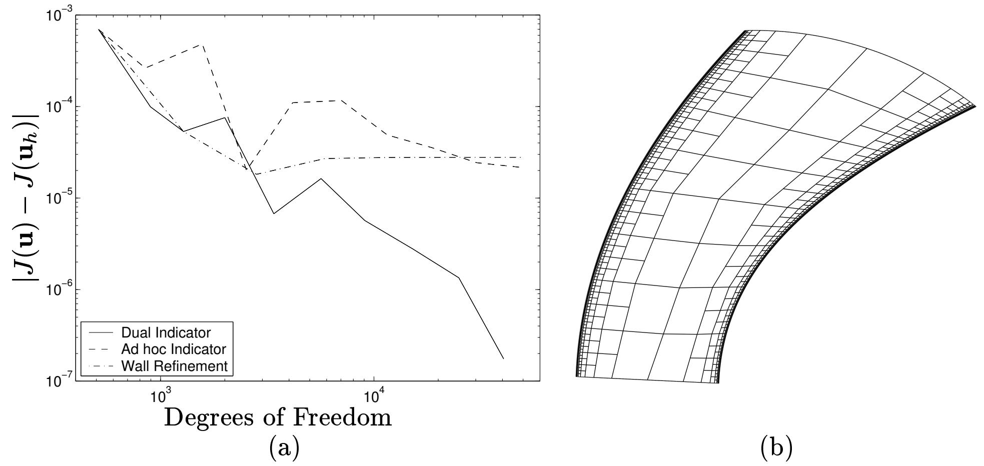

FIG. 7.10. *Example 3. (a) Convergence of* $|J(\mathbf{u}) - J(\mathbf{u}_h)|$ *using the dual and* ad hoc *error indicators, as well as simply refining elements near the channel walls; (b) Mesh constructed by only refining elements near the channel walls with* 3056 *elements and* 48896 *degrees of freedom* ($|J(\mathbf{u}) - J(\mathbf{u}_h)| = 2.789 \times 10^5$).

indicator is used. Additionally, in Figure 7.10(a) we also compare the performance of our weighted *a posteriori* error indicator $|\hat{\eta}_\kappa|$ with a simple–minded mesh refinement algorithm which only refines elements adjacent to the channel walls, cf. Figure 7.10(b). Given the choice of the target functional, and the structure of the meshes produced using $|\hat{\eta}_\kappa|$, one may expect that this approach should work quite well without the need to solve the dual problem. However, we now see that after an initial reduction in the error in the computed functional $J(\cdot)$, $|J(\mathbf{u}) - J(\mathbf{u}_h)|$ becomes $\mathcal{O}(1)$ under additional mesh refinement. This is attributed to the fact that while it is important to refine the mesh near the channel walls in order to reduce the error in the target functional $J(\cdot)$, some mesh refinement is also required in the interior of the computational domain. Here, the weighted *a posteriori* error indicators $|\hat{\eta}_\kappa|$ give us information about not only where to refine the mesh, but also by how much; this leads to the consistent reduction in $|J(\mathbf{u}) - J(\mathbf{u}_h)|$ observed in Figure 7.10(a) as the finite element mesh is adaptively refined.

7.4. Supersonic compression corner. In this final example we study the formation of an oblique shock when supersonic flow is deflected by a sharp object or wedge. Here, we consider a Mach 3 flow with inflow density $\rho = 1$ and pressure $p = 1$, over a compression corner of angle α; this leads to the development of a shock wave at an angle β, cf. Figure 7.11. By employing the Rankine–Hugoniot jump conditions, the analytical solution to this problem may be determined for a given α, see Brooksbanks [7] for details. Here, we select the wedge angle $\alpha = 9.5°$; thereby, the angle of the shock is given by $\beta = 26.9308°$. Furthermore, the true solution on the left– and right–hand side of the shock, in terms of conserved variables $(\rho, \rho u, \rho v, \rho E)$, are given by

$$\mathbf{u}_{\text{left}} = \begin{bmatrix} 1 \\ 3.5496 \\ 0 \\ 8.8 \end{bmatrix} \quad \text{and} \quad \mathbf{u}_{\text{right}} = \begin{bmatrix} 1.6180 \\ 5.2933 \\ 0.8858 \\ 13.8692 \end{bmatrix},$$

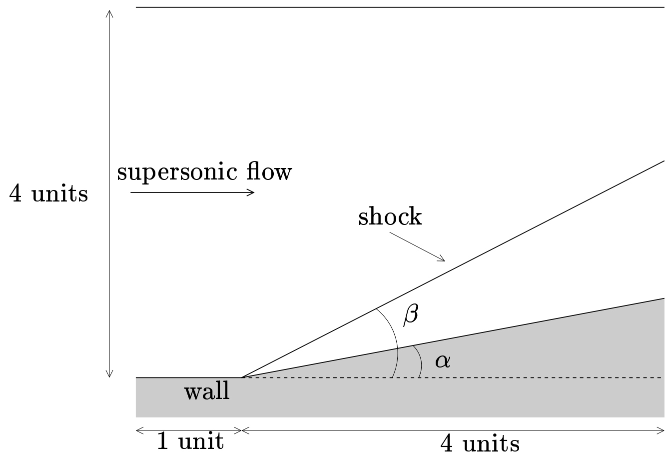

FIG. 7.11. *Example 4. Geometry for the supersonic compression corner.*

Elements	DOF	$J(\mathbf{u}) - J(\mathbf{u}_h)$	$\sum_\kappa \hat{\eta}_\kappa$	θ_1	$\sum_\kappa \lvert\hat{\eta}_\kappa\rvert$	θ_2
20	320	-3.428e-01	2.771e-02	-0.08	8.565e-02	0.25
35	560	-3.194e-01	-4.315e-02	0.14	8.134e-02	0.25
65	1040	-3.320e-01	-6.235e-02	0.19	7.675e-02	0.23
128	2048	-2.666e-01	-1.356e-01	0.51	1.819e-01	0.68
227	3632	-2.164e-01	-1.665e-01	0.77	2.142e-01	0.99
386	6176	-3.272e-03	-8.919e-02	27.26	2.094e-01	63.99
677	10832	1.686e-02	1.077e-02	0.64	5.179e-02	3.07
1175	18800	-5.475e-03	-5.887e-03	1.08	2.130e-02	3.89
1964	31424	-3.383e-04	-3.635e-04	1.07	3.671e-03	10.85
3293	52688	-4.208e-06	-3.837e-06	0.91	3.000e-04	71.30
5516	88256	4.551e-07	5.056e-07	1.11	2.079e-05	45.67

TABLE 7.4

Example 4A. Adaptive algorithm for the supersonic compression corner; point evaluation of the density in front of the shock.

respectively.

Throughout this section, we set the shock capturing parameters C_ε and β, appearing in (3.4), equal to 1/50 and 1/10, respectively. In Table 7.4, we show the performance of our adaptive algorithm when the target functional is chosen to be the value of the density just in front of the shock; more precisely, here

$$J(\mathbf{u}) = \rho(5, 2.05).$$

As in the previous examples, we again see that the quality of the computed error representation formula (5.4) is extremely good with θ_1 tending to unity, as the mesh is adaptively refined. Furthermore, the resulting Type I *a posteriori* bound (5.3) over–estimates the true error in the computed target functional by about one–two orders of magnitude.

We end this example by considering the more interesting case of estimating the value of the density just behind the shock; to this end, we select

$$J(\mathbf{u}) = \rho(5, 2.01).$$

Elements	DOF	$J(\mathbf{u}) - J(\mathbf{u}_h)$	$\sum_\kappa \hat{\eta}_\kappa$	θ_1	$\sum_\kappa \lvert\hat{\eta}_\kappa\rvert$	θ_2
20	320	2.548e-01	3.952e-02	0.16	9.546e-02	0.37
35	560	2.652e-01	-1.728e-02	-0.07	9.185e-02	0.35
68	1088	2.226e-01	-1.148e-02	-0.05	4.927e-02	0.22
134	2144	1.723e-01	6.407e-02	0.37	1.254e-01	0.73
209	3344	1.259e-01	1.007e-01	0.80	1.369e-01	1.09
389	6224	6.044e-02	9.786e-02	1.62	1.180e-01	1.95
650	10400	-1.453e-02	-1.538e-02	1.06	5.050e-02	3.48
1124	17984	5.425e-04	4.530e-03	8.35	3.220e-02	59.36
1997	31952	4.470e-04	3.006e-03	6.73	2.733e-02	61.15
3395	54320	2.888e-04	1.405e-03	4.86	2.401e-02	83.15

TABLE 7.5

Example 4B. Adaptive algorithm for the supersonic compression corner; point evaluation of the density behind the shock.

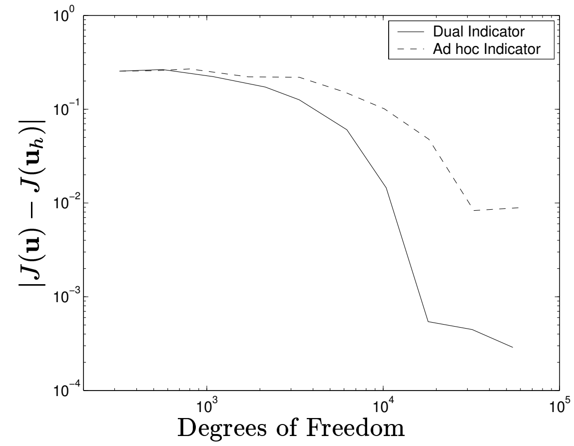

FIG. 7.12. *Example 4. Convergence of* $|J(\mathbf{u}) - J(\mathbf{u}_h)|$ *using the dual and* ad hoc *error indicators.*

The performance of the adaptive algorithm in this case is presented in Table 7.5. Here, we now see that while the computed *a posteriori* estimate still remains a reliable upper–bound on the size of the error in the computed functional, the ratio of the (computed) error representation formula $\hat{\mathcal{E}}_\Omega$ and $J(\mathbf{u}) - J(\mathbf{u}_h)$ no longer tends to one as the finite element mesh is refined; indeed, here we see that (ignoring the first few refinement steps) θ_1 lies in the interval $(0.8, 8.35)$. This degradation in the quality of the computed error representation formula when the point of evaluation lies behind the shock is attributed to the effects of the linearisation error and the error in the approximation to the Fréchet derivative of the semilinear form $\mathcal{N}(\cdot,\cdot)$ (with respect to its first argument), becoming large in the vicinity of the shock. In this case, the weighting terms involving the difference between the dual solution and its projection/interpolant (cf. (5.3)) are poorly approximated in the neighbourhood of the shock, where the residual terms R_h and r_h, and the shock capturing term $\varepsilon\nabla\mathbf{u}_h$ are large, thereby leading to a poor approximation of the true error in the target functional $J(\cdot)$. We note that this does *not* occur if the target functional is selected upstream of the shock, since then the dual solution no longer interacts with the shock; thereby, in the neighbourhood of the shock, the weighting terms are negligibly

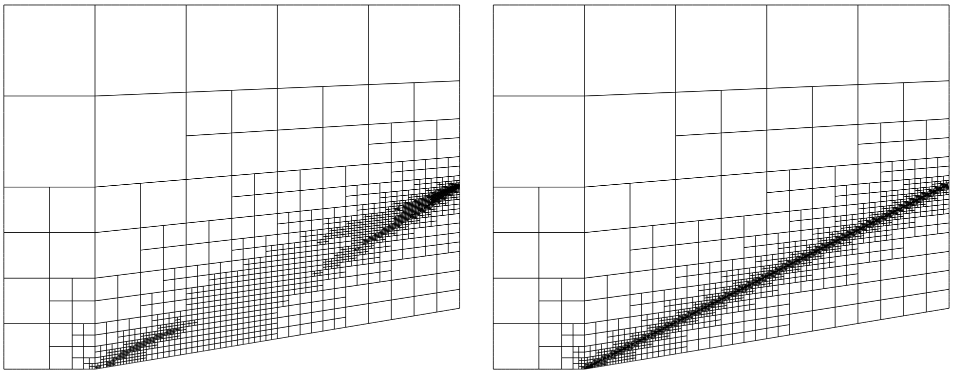

(a) (b)

FIG. 7.13. *Example 4B. (a) Mesh constructed using dual error indicator with* 3395 *elements and* 54320 *degrees of freedom* ($|J(\mathbf{u}) - J(\mathbf{u}_h)| = 2.888 \times 10^{-4}$)*; (b) Mesh constructed using* ad hoc *error indicator with* 3821 *elements and* 61136 *degrees of freedom* ($|J(\mathbf{u}) - J(\mathbf{u}_h)| = 8.938 \times 10^{-3}$).

small, and the computed error representation formula is extremely good, cf. above. Thus, in order to guarantee the quality of the computed error representation formula, additional computational work is required to reduce the effects of the linearisation error, the error stemming from the approximation of $\mathcal{N}'_{\mathbf{u}}(\cdot, \mathbf{v})$, $\mathbf{v} \in V$ fixed, and the error generated in the numerical approximation of the (approximate) dual problem; this is beyond the scope of the current paper, but will be considered in [18].

Notwithstanding this reduction in the quality of the computed error representation formula when the point of interest lies behind the shock, the adaptively refined meshes generated by employing the weighted error indicator $|\hat{\eta}_\kappa|$ are much more economical than those produced using the traditional *ad hoc* error indicator $\eta_\kappa^{\mathrm{adhoc}}$. Indeed, in Figure 7.12 we clearly observe the superiority of the former error indicator; on the final mesh the true error in the computed functional is over an order of magnitude smaller when the weighted error indicator is employed.

Finally, in Figure 7.13 we show the meshes produced using both error indicators. Here, we see that the mesh constructed using $\eta_\kappa^{\mathrm{adhoc}}$ is concentrated in the neighbourhood of the shock, cf. Example 1. In contrast, the mesh produced using the weighted error indicator $|\hat{\eta}_\kappa|$ only refines the mesh in the vicinity of the top and bottom parts of the shock. To gain insight into the structure of this mesh, in Figures 7.14(a) and 7.14(b) we show the dual solutions corresponding to Example 4A and Example 4B, respectively; for clarity, here we show the z_1 component of the dual solutions computed on globally refined meshes. The dual solution corresponding to the point evaluation of the density in front of the shock, see Figure 7.14(a), consists of three 'spikes', labelled 1, 2 and 3 in Figure 7.14(a), originating from the point of interest. These spikes are transported upstream along the characteristics corresponding to the three eigenvalues $\bar{v}$ and $\bar{v} \pm c$, with $\bar{v} = \sqrt{u^2 + v^2}$ denoting the velocity of the gas and $c = \sqrt{\gamma p/\rho}$ the speed of sound. We note that the support of this dual solution does not intersect the region of the computational domain where the shock in the primal solution is located. In contrast, the support of dual solution corresponding to the point evaluation of the density behind the shock, see Figure 7.14(b), now intersects the region containing the shock; here, we observe that z_1 has a rather complicated structure. The two upper spikes of the dual solution both cross the shock in the neighbourhood of the point of evaluation. At their crossing points they again each split into a further three spikes.

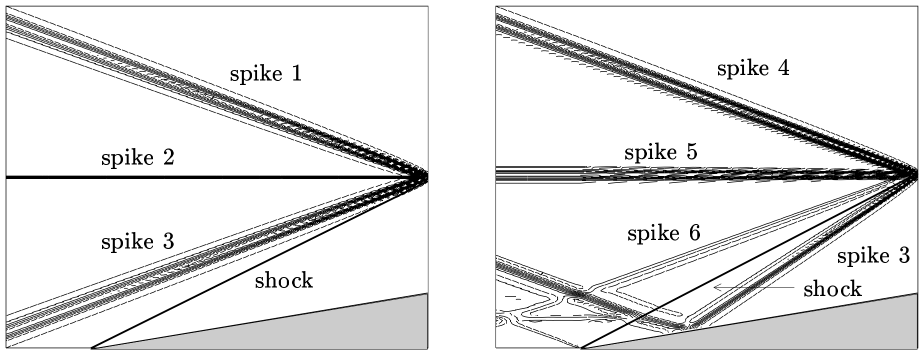

(a) (b)

FIG. 7.14. *Example 4A and 4B. z_1 component of dual solution for the supersonic compression corner for point evaluation of the density (a) in front of shock (b) behind shock.*

These six spikes correspond to the three pairs of spikes, labelled spikes 4, 5 and 6 in Figure 7.14(b); the two spikes in each pair cannot be distinguished on the resolution shown, as they are extremely close together. Spike 3, corresponding to the same spike in Figure 7.14(a), is reflected off the inclined wall and crosses the shock at its bottom part. A comparison of the dual solution in Figure 7.14(b) and the mesh in Figure 7.13(a) shows that the mesh has only been refined along the support of spikes 3 and 6 in the vicinity of the top part of the shock, and in the neighbourhood of the point where spike 3 crosses the bottom part of the shock. This demonstrates that it is not necessary to refine the entire shock in this example to gain an accurate evaluation of the target functional under consideration, but only those parts that influence the value of the target functional either by material transport, cf. eigenvalue $\bar{v}$, or by information transported by the sound waves, cf. eigenvalues $\bar{v} \pm c$. Indeed, as seen in Figure 7.12, the meshes produced using our weighted error indicator are much more economical for computing the value of the target functional than meshes produced using the traditional *ad hoc* error indicator.

8. Concluding remarks. In this article, we have developed the *a posteriori* error analysis of the discontinuous Galerkin finite element method for systems of nonlinear hyperbolic conservation laws. In particular, by employing a duality argument, we have derived so–called weighted or Type I *a posteriori* error bounds for general linear and nonlinear target functionals of the solution. Numerical experiments have been presented to illustrate the quality of the approximate error representation formula, when the (approximate) dual problem is approximated numerically. Moreover, comparisons with traditional *ad hoc* error indicators which stem from Type II *a posteriori* error bounds have clearly demonstrated the superiority of exploiting weighted *a posteriori* error indicators to guide adaptive mesh refinement; in all examples, the error in the computed target functional is significantly smaller for a given number of degrees of freedom when the proposed error indicator is employed. Furthermore, Type II *a posteriori* estimates will in general not be sharp; indeed, the Type I *a posteriori* bound derived from the error representation formula by simply employing the triangle inequality already over–estimates the error in the computed target functional by at least an order of magnitude.

Several open questions still remain; most notably the issue of well–posed of the dual problem which, although being linear, is a non-standard hyperbolic problem in the sense that the coefficients may be discontinuous. The only known analytical results, which hold in the one–dimensional case, are those by Tadmor [31]. In addition, further work concerning the quality of the (approximate) error representation formula in the presence of shocks still needs further numerical investigation, cf. [18].

Acknowledgments. Ralf Hartmann acknowledges the financial support of the DFG Priority Research Program and the SFB 359 at the IWR, University of Heidelberg. Paul Houston acknowledges the financial support of the EPSRC (Grant GR/N24230). The authors wish to express their sincere gratitude to Professor Tim Barth (NASA Ames Research Center) for providing the algorithm used to generate the analytical solution to Ringleb's flow. Finally, we wish to thank Professor Rolf Rannacher (University of Heidelberg) and Professor Endre Süli (University of Oxford) for their helpful comments.

REFERENCES

[1] W. Bangerth, R. Hartmann, and G. Kanschat, `deal.II` *Differential Equations Analysis Library, Technical Reference.* IWR, University of Heidelberg, Apr. 2001. Available from the URL: `http://gaia.iwr.uni-heidelberg.de/~deal/`.

[2] W. Bangerth and G. Kanschat, *Concepts for object-oriented finite element software – the deal.II library.* Preprint 99-43, SFB 359, University of Heidelberg, Oct. 1999.

[3] F. Bassi and S. Rebay, *High–order accurate discontinuous finite element solution of the 2D Euler equations.* J. Comput. Phys. 138:251–285, 1997.

[4] R. Becker and R. Rannacher, *A feed–back approach to error control in finite element methods: Basic analysis and examples.* East–West J. Num. Math., 4:237–264, 1996.

[5] R. Biswas, K.D. Devine and J. Flaherty, *Parallel, adaptive finite element methods for conservation laws.* Appl. Numer. Math. 14:255–283, 1994.

[6] F. Brezzi, P. Houston, D. Marini and E. Süli, *Modeling subgrid viscosity for advection–diffusion problems.* Comput. Meth. in Appl. Mech. and Engrg., 190(13-14):1601–1610, 2000.

[7] E. Brooksbanks, *Recent Progress on Vortex Shedding Behind Turbine Blades.* Ph.D. thesis, University of Leicester (in preparation).

[8] G. Chiocchia, *Exact solutions to transonic and supersonic flows.* Technical Report AR-211, AGARD, 1985.

[9] B. Cockburn, S. Hou, and C. Shu, *TVB Runge–Kutta local projection discontinuous Galerkin finite element method for conservation laws IV: The multidimensional case.* Math. Comp., 54:545–581, 1990.

[10] B. Cockburn, G.E. Karniadakis and C.-W. Shu, *The development of discontinuous Galerkin methods.* In: B. Cockburn, G. Karniadakis, and C.-W. Shu (Eds.) Discontinuous Galerkin Finite Element Methods. Lecture Notes in Computational Science and Engineering, Volume 11. Springer-Verlag 2000.

[11] B. Cockburn and C.-W. Shu, *The Runge–Kutta discontinuous Galerkin finite element method for conservation laws V: Multidimensional systems.* J. Comput. Phys. 141:199–224, 1998.

[12] K. Eriksson, D. Estep, P. Hansbo, and C. Johnson, *Introduction to adaptive methods for differential equations.* Acta Numerica, 105–158, 1995.

[13] C. Führer and R. Rannacher, *An adaptive streamline–diffusion finite element method for hyperbolic conservation laws.* East–West J. Numer. Math. 5:145–162, 1997.

[14] J. Giannakouros and G.E. Karniadakis, *Spectral element–FCT method for scalar hyperbolic conservation laws.* Int. J. Num. Meth. Fluids, 14:707, 1992.

[15] D. Gottlieb and J. S. Hesthaven, *Spectral methods for hyperbolic problems.* J. Comput. Appl. Math. (to appear).

[16] P. Hansbo and C. Johnson, *Streamline diffusion finite element methods for fluid flow.* von Karman Institute Lectures, 1995.

[17] R. Hartmann, *Adaptive FE–methods for conservation equations.* In: G. Warnecke and H. Freistühler (Eds.) Proc. Eighth International Conference on Hyperbolic Problems. Theory, Numerics, Applications (HYP2000). Birkhäuser, Basel. (to appear).

[18] R. Hartmann and P. Houston, *A posteriori error estimation for nonlinear hyperbolic conservation laws involving discontinuous solutions.* In preparation.

[19] F.-K. Hebeker and R. Rannacher, *An adaptive finite element method for unsteady convection–dominated flows with stiff source terms.* SIAM J. Sci. Comp., 21:799–818, 1999.

[20] P. Houston, R. Hartmann and E. Süli, *Adaptive Discontinuous Galerkin Finite Element Methods for Compressible Fluid Flows.* In M. Baines, editor, *Numerical Methods for Fluid Dynamics VII*, (to appear).

[21] P. Houston, R. Rannacher and E. Süli, *A posteriori error analysis for stabilised finite element approximations of transport problems.* Comput. Meth. Appl. Mech. Engrg., 190(11-12):1483–1508, 2000.

[22] P. Houston, Ch. Schwab, and E. Süli, *Stabilized hp-finite element methods for first–order hyperbolic problems.* SIAM J. Numer. Anal. 37(5):1618-1643, 2000.

[23] P. Houston and E. Süli, *hp–Adaptive discontinuous Galerkin finite element methods for first–order hyperbolic problems.* Leicester University Technical Report 2000/31, 2000. (Submitted for publication). Available from the URL `http://www.mcs.le.ac.uk/~phouston/`.

[24] J. Jaffre, C. Johnson and A. Szepessy, *Convergence of the discontinuous Galerkin finite element method for hyperbolic conservation laws.* Math. Models Methods Appl. Sci. 5(3):367–386, 1995.

[25] C. Johnson and A. Szepessy, *Adaptive finite element methods for conservation laws.* Commun. Pure Appl. Math. 48:199–243, 1995.

[26] D. Kröner, *Numerical Schemes for Conservation Laws.* Wiley-Teubner, 1997.

[27] M.G. Larson and T.J. Barth, *A posteriori error estimation for discontinuous Galerkin approximations of hyperbolic systems.* In: B. Cockburn, G. Karniadakis, and C.-W. Shu, editors, *Discontinuous Galerkin Finite Element Methods.* Lecture Notes in Computational Science and Engineering, Volume 11. Springer–Verlag 2000.

[28] R. Rannacher, *Adaptive finite element methods*, in H. Bulgak and C. Zenger, eds., Proc. NATO-Summer School *Error Control and Adaptivity in Scientific Computing*, Kluwer, Academic Publishers, 247–278, 1998.

[29] E. Süli, *A posteriori error analysis and adaptivity for finite element approximations of hyperbolic problems.* In: D. Kröner, M. Ohlberger and C. Rohde (Eds.) An Introduction to Recent Developments in Theory and Numerics for Conservation Laws. Lecture Notes in Computational Science and Engineering. Volume 5, pages 123–194. Springer-Verlag, 1998.

[30] E. Süli, P. Houston and B. Senior, *hp–Discontinuous Galerkin finite element methods for hyperbolic problems: error analysis and adaptivity.* In M. Baines, editor, *Numerical Methods for Fluid Dynamics VII*, (to appear).

[31] E. Tadmor, *Local error estimates for discontinuous solutions of nonlinear hyperbolic equations.* SIAM J. Numer. Anal., 28:891–906, 1991.

[32] E. Toro, *Riemann solvers and numerical methods for fluid dynamics.* Springer–Verlag, 1997.